23132

UCRL-JC-126777
PREPRINT

Aromatic and Polycyclic Aromatic Hydrocarbon Formation in a Laminar Premixed n-Nutane Flame

N.M. Marinov
W.J. Pitz
C.K. Westbrook
M.J. Castaldi
S.M. Senkan
C.F. Melius

This paper was prepared for submittal to
Combustion and Flame

March 1997

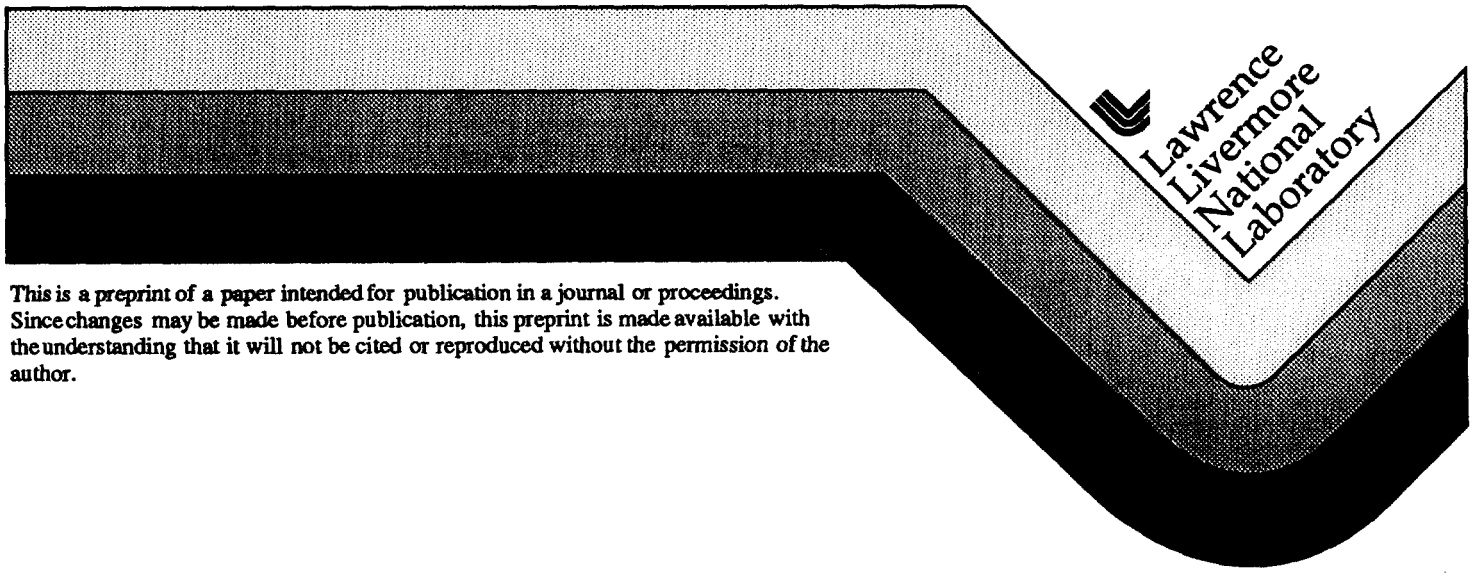

This is a preprint of a paper intended for publication in a journal or proceedings. Since changes may be made before publication, this preprint is made available with the understanding that it will not be cited or reproduced without the permission of the author.

DISCLAIMER

This document was prepared as an account of work sponsored by an agency of the United States Government. Neither the United States Government nor the University of California nor any of their employees, makes any warranty, express or implied, or assumes any legal liability or responsibility for the accuracy, completeness, or usefulness of any information, apparatus, product, or process disclosed, or represents that its use would not infringe privately owned rights. Reference herein to any specific commercial product, process, or service by trade name, trademark, manufacturer, or otherwise, does not necessarily constitute or imply its endorsement, recommendation, or favoring by the United States Government or the University of California. The views and opinions of authors expressed herein do not necessarily state or reflect those of the United States Government or the University of California, and shall not be used for advertising or product endorsement purposes.

Aromatic and Polycyclic Aromatic Hydrocarbon Formation in a Laminar Premixed n-Butane Flame

Nick M. Marinov[1], William J. Pitz[1], Charles K. Westbrook[1], Marco J. Castaldi[2], Selim M. Senkan[2], and Carl F. Melius[3]

[1]Lawrence Livermore National Laboratory, Livermore, CA 94551
[2]University of California at Los Angeles, Los Angeles, CA 90024
[3]Sandia National Laboratories, Livermore, CA 94551

Correspondence should be addressed to:

Nick M. Marinov
Lawrence Livermore National Laboratory
P.O. Box 808
Mail stop: L-014
Livermore, CA 94550
Phone: (510) 424-5463
Fax: (510) 422-2644
Internet: marinov@llnl.gov

Shortened Running Title: Aromatic and PAH Formation in a n-Butane Flame

Aromatic and Polycyclic Aromatic Hydrocarbon Formation in a Laminar Premixed N-Butane Flame

Nick M. Marinov[1], William J. Pitz[1], Charles K. Westbrook[1], Marco J. Castaldi[2], Selim M. Senkan[2], and Carl F. Melius[3]

[1]Lawrence Livermore National Laboratory, Livermore, CA 94551
[2]University of California at Los Angeles, Los Angeles, CA 90024
[3]Sandia National Laboratories, Livermore, CA 94551

Abstract

Experimental and detailed chemical kinetic modeling has been performed to investigate aromatic and polycyclic aromatic hydrocarbon (PAH) formation pathways in a premixed, rich, sooting, n-butane-oxygen-argon burner stabilized flame. An atmospheric pressure, laminar flat flame operated at an equivalence ratio of 2.6 was used to acquire experimental data for model validation. Gas composition analysis was conducted by an on-line gas chromatograph / mass spectrometer (GC/MS) technique. Measurements were made in the main reaction and post-reaction zones for a number of low molecular weight species, aliphatics, aromatics, and polycyclic aromatic hydrocarbons (PAHs) ranging from two to five-fused aromatic rings.

Reaction flux and sensitivity analysis were used to help identify the important reaction sequences leading to aromatic and PAH growth and destruction in the n-butane flame. Reaction flux analysis showed the propargyl recombination reaction was the dominant pathway to benzene formation. The consumption of propargyl by H-atoms was shown to limit propargyl, benzene, and naphthalene formation in flames as exhibited by the large negative sensitivity coefficients. Naphthalene and phenanthrene production were shown to be plausibly formed through reactions involving resonantly stabilized cyclopentadienyl and indenyl radicals.

Many of the low molecular weight aliphatics, combustion by-products, aromatics, branched aromatics, and polycyclic aromatics were fairly well simulated by the model. Additional work is required to understand the formation mechanisms of phenyl acetylene, pyrene, and fluoranthene in the n-butane flame.

Introduction

Butane is a naturally occurring alkane that is produced by the fractionation of crude oil in refinery operations or during natural gas processing. One of the uses of butane is to form ethylene by thermal cracking [1], which is used as the major feedstock to manufacture plastics. It can also be dehydrogenated to make 1,3-butadiene which is a precursor to rubber. Large amounts of n-butane are consumed as fuel or a fuel component in internal combustion engines, industrial burners, and residential heating. Unlike hydrocarbon fuels with simpler structures such as methane or ethane, the thermochemical and combustion properties of n-butane are similar in many ways to more complex practical fuels. In addition to being a fuel component in gasoline, butane is used to control the volatility of the final product. It comprises about 6 to 8 percent by volume in gasoline and is the second largest component behind iso-pentane. Liquefied petroleum gas (LPG), which is a mixture of butane and propane in a typical ratio of 60:40, is being examined as an alternative to gasoline in motor vehicles. As regulations become stricter, it is possible that LPG will increase in consumption because of its ability to burn cleaner than gasoline. Butanes are a component in natural gas, comprising about 0.4 molar percent average across the U. S. [2]. N-butane also is contained at an average of 1.7% in refinery fuel gas which is used in large quantities as a fuel in refineries [3]. Lastly, n-butane is also used in other chemical operations such as the manufacture of acetic acid, maleic anhydride and isobutane and as a solvent in liquid - liquid extraction of heavy oils in a deasphalting process.

There are fundamental and practical reasons for examining the fuel-rich oxidation process of n-butane. The reaction sequences that lead to aromatic and polycyclic aromatic hydrocarbon (PAH) formation within a n-butane flame comprise a very complicated and poorly understood process. The fused-ring compounds have been suspected to be mutagenic and carcinogenic in nature and currently their emissions are subject to regulatory control as mandated by the 1990 Clean Air Act Amendments. It has become necessary to have a full understanding of the chemistry involved when n-butane is used in combustion

as regulations on pollutant emissions are becoming stricter. This understanding will allow industry and regulatory agencies to better evaluate the feasibility and relationship between the combustion process and pollutant emissions.

Many previous investigations have focused on the formation of aromatics and PAH in premixed, laminar, fuel-rich flames for aliphatic fuels. Some of these have been experimental investigations [4-6] while others have combined experiments with chemical kinetic modeling [7-10]. We have recently investigated aromatic and PAH formation in methane, ethane, ethylene, and propane flames [11-13]. The chemical kinetic mechanism used in the present study is based on one developed previously to describe these flames. The important, new features in the chemical kinetic mechanism that we have been developing in this series of studies include the formation of two-ring and three-ring PAH via the reaction of resonantly stabilized radicals.

In this work, we have performed an experimental and modeling investigation of a premixed, rich, laminar, n-butane-oxygen-argon flame with the objective of identifying the important reaction sequences that lead to the formation of aromatics, branched aromatics, and polycyclic aromatic hydrocarbons. As shown later, the modeling effort performed fairly well when predicting the aromatic and PAH profiles as measured in the n-butane flame. In the following sections, the experimental apparatus is described, the chemical kinetic model is discussed, and the experimental and modeling results are compared.

Experimental

The experimental system has been described in a previous publication [11], and thus, only a brief summary will be given here. The atmospheric-pressure, premixed, laminar, flat-flame of 15.67%C_4H_{10}/ 39.64%O_2/ 45.04%Ar (Φ=2.6, 9.34E-3 g/cm2-sec) mass flow rate through the burner) was stabilized over a cooled 50 mm diameter porous bronze burner. The flame was protected from the ambient environment by use of aconcentric

shield gas stream of argon. Gas sampling was performed using two quartz microprobes operated at 50 Torr internal pressure. The two probes differed in orifice diameter so as to sample gases in the main reaction zone and in the sooty region of the post reaction zone. This combined sampling approach coupled with the on-line gas chromatograph/mass spectrometer (GC/MS) gas analysis technique allowed for spatially resolved species measurements of the n-butane flame.

The gas sampling system, which include the probe, silica-lined tubing, and GC valves were maintained above 300°C and at sub-ambient pressures to minimize the condensation and/or adsorption of PAHs on surfaces. The sampling system was also checked for possible catalytic activity at 300°C by passing unburned gas mixtures; none was observed.

Identification of species were accomplished by matching both the gas chromatographic retention times to pure components and mass spectral fragmentation patterns to standard MS libraries. The estimated accuracy for the major species is ±15% and ±20% for the remaining ones. The relative ionization cross section (IC) method was used to quantify those species whose calibration standards were not available [14]. Those species whose concentrations were determined by the relative ionization cross section method were C_3H_4 (allene and propyne), C_4H_2 (diacetylene), C_4H_4 (vinylacetylene), C_4H_6 (1,2 or 1,3-butadiene, and 1 or 2-butyne), C_4H_8 (1 or 2- butene), c-C_5H_6 (cyclopentadiene), $C_6H_5CH_3$ (toluene), $C_6H_5C_2H_5$ (ethylbenzene), $C_6H_5C_2H_3$ (styrene), $C_6H_5C_2H$ (phenylacetylene), $CH_3C_6H_4CH_3$ (o-xylene), C_9H_8 (indene), $C_{11}H_{10}$ (methyl napthalene), $C_{12}H_8$ (acenapthalene and biphenylene), $C_{12}H_{10}$ (biphenyl), and $C_{18}H_{10}$ (cyclopenta[cd]pyrene and benzo[ghi]fluoranthene). The uncertainty attributed to these species measurements is at least a factor of two.

Temperature profiles were measured by using 0.075 mm Pt-Pt/13%Rh thermocouple wires with a bead diameter of ca. 0.15 mm and were performed immediately after the concentration measurements. The thermocouple bead was freshly coated by silica

and vitrified before each experiment to minimize catalysis. The thermocouple was kept in the flame for as little time as possible to prevent excessive soot buildup. Any accumulated soot was burned off by moving the thermocouple to the non-sooting region of the flame. The flame temperature measurements were corrected for radiation losses. We have assumed an emissivity value of 0.90. This results in a maximum correction in temperature of ca. 105 K at 1.5 mm above the burner surface. The uncertainty in the flame temperature is estimated to be ±100 K. The temperature profile used in this flame study is shown in Figure 1.

Computational Model and Mechanism

The computational model used in this study is the Sandia laminar one-dimensional premixed flame (CHEMKIN/PREMIX) code [15,16]. The PREMIX code computes the species profiles for a burner-stabilized premixed laminar flame using the cold mass flow rate through the burner, feed-gas composition, pressure, and an estimated solution profile as input. The program can compute the temperature profile however heat losses to the burner surface and the external environment are unknown, and therefore an experimentally determined temperature profile is used as input. The code solves the governing equations for a steady, isobaric, 1-D burner-stabilized premixed laminar flame by using a finite difference / modified-Newton method scheme. The numerical computations performed in this study were carried out using the DEC ALPHA 440 Model series computer.

Thermochemical information was primarily obtained from the Chemkin thermodynamic database [17-20]. Thermodynamic properties for those species not found in the literature or the Chemkin thermodynamic database were estimated by group additivity and difference methods [21-23]. These estimated specific heats, standard state enthalpies, and standard state entropies data were fitted for the 300K to 1500K temperature range and extrapolated to 5000K using the Harmonic Oscillator Equation and Exponential Function

methods in THERM [24]. The THERM program generates the fourteen polynomial coefficients as used in the NASA Complex Chemical Equilibrium program [25]. The compiliation of the thermochemical data in polynomial coefficient form may be obtained from the corresponding author or the data has been presented elsewhere [11]. Additional or modified thermodynamic parameters used in this study are given in Table 1.

Transport properties were obtained from the Sandia CHEMKIN transport data base [28] as found in the TRANDAT file of the Sandia TRANFIT program. Transport properties for species not found in the database were obtained using methods described by Wang and Frenklach [29].

The detailed chemical kinetic model was primarily composed of the Miller-Melius [30] benzene formation submechanism, Tsang's propane and propene chemical kinetic reviews [31,32], Pitz-Westbrook n-butane submechanism [33], the Emdee-Brezinsky-Glassman toluene and benzene oxidation submechanisms [34], and the Wang-Frenklach HACA reaction set [35] for PAH formation. This chemical kinetic model was used as a starting point for mechanism development. Subsequent changes to the baseline model were made to include new information from the chemical kinetics literature, and the model was extended to allow prediction of methyl-substituted aromatics, and for alternative chemical pathways leading to multi-fused aromatic ring structures. The detailed chemical kinetic model used in this study consists of 680 reactions and 156 species. The model was previously presented and extended in our earlier experimental and modeling investigation of premixed methane, ethane, ethylene, and propane burner stabilized flames. Although these fuel-rich flames are sooting, we have not as yet included a submodel to treat soot production and destruction. Additonal reactions or modifications to the reaction rate parameters from Marinov [11] are presented in Table 2.

In our earlier studies we had proposed several reaction steps involving the combination of resonantly stabilized free radicals. Propargyl, allyl, 1-methylallenyl, and cyclopentadienyl radicals were identified as an important aromatic and PAH precursor

species which eventually lead to benzene, toluene, xylene, naphthalene, and phenanthrene formation in flames. These resonantly stabilized radicals play an important role in aromatic and PAH formation as these species can build up in concentration within the flame since they are relatively resistant to oxidation by O_2. In this study, we have continued to investigate the role of resonantly stabilized radicals in aromatic, branched aromatic and polycyclic aromatic hydrocarbon formation in a premixed, rich, laminar, n-butane-oxygen argon flame.

Analysis and Comparison of Modeling Results to the Flame Data

The modeling results are compared to the experimental results first for the low molecular weight species, and then for the aromatic and PAH species. The key chemical reactions leading to different stable intermediates are identified by reaction flux analysis.

Low Molecular Weight Species

The measured and predicted C_4H_{10}, and H_2O concentrations are shown in figure 1(a). For distances greater than 0.10cm above the burner surface, the model indicated a faster n-butane consumption rate than indicated by the experiment while the O_2 and H_2O profiles were fairly well simulated. The n-butane (C_4H_{10}) was primarily consumed by unimolecular decomposition, $C_4H_{10} \leftrightarrow C_3H_7+CH_3$ (approximately 35%), and abstraction by H-atom, $C_4H_{10}+H \leftrightarrow sC_4H_9+H_2$ (approximately 30%), reactions. The remaining fraction of n-butane was consumed by $C_4H_{10} \leftrightarrow C_2H_5+C_2H_5$ (approximately 20%) and $C_4H_{10}+H \leftrightarrow pC_4H_9+H_2$ (approximately 15%). The $C_4H_{10}+H \leftrightarrow sC_4H_9+H_2$ reaction dominates in the first millimeter of the flame while $C_4H_{10} \leftrightarrow nC_3H_7+CH_3$ and $C_4H10 \leftrightarrow C_2H_5+C_2H_5$ dominates in the remaining portion of the flame. The molecular oxygen (O_2) was primarily consumed by $HCO+O_2 \leftrightarrow CO+HO_2$ and secondarily by

$H+O_2 \leftrightarrow OH+O$ from the burner surface to 0.15cm above the burner surface. For distances greater than 0.15cm, the model showed O_2 being consumed primarily by $H+O2 \leftrightarrow OH+O$ with secondary consumption contributions due to $HCO+O_2 \leftrightarrow CO+HO_2$ and $C_2H_3+O_2 \leftrightarrow C_2H_2+HO_2$. The $C_2H_5(+M) \leftrightarrow C_2H_4+H(+M)$ and $HCO+M \leftrightarrow H+CO+M$ reactions were determined to be the important H-atom sources for O_2 removal. The model well predicted the water (H_2O) profile in the main and post-reaction zones. The H2O is formed by $H_2+OH \leftrightarrow H_2O+H$, while the H_2 needed for H_2O production is formed by $C_4H_{10}+H \leftrightarrow pC_4H_9+H_2$ and $C_4H_{10}+H \leftrightarrow sC_4H_9+H_2$ in the main reaction zone and by $C_2H_4+H \leftrightarrow C_2H_3+H_2$ in the post reaction zone.

In figure 1(b), the measured and predicted CO, CO_2, and H_2 concentrations are shown. The CO was well predicted by the model in the main reaction and post-reaction zones, and its dominant production source was $HCO+M \leftrightarrow H+CO+M$. Carbon dioxide ($CO_2$) is formed by $HCCO+O_2 \leftrightarrow CO_2+HCO$ and its concentration profile was over predicted by a factor of two. Molecular hydrogen (H_2) measurements show an unexpected shape and we do not know if the differences between the predicted and measured profile shape are of any significance. It must be mentioned that the H_2 concentration profile was calculated based on an H-atom balance, and therefore the accuracy of the H_2 profile determined by this approach is called into question. The H_2 profile was determined in this way due to problems of the peak separation for the molecular hydrogen.

In figure 2(a), the measured and predicted methane (CH_4), acetylene (C_2H_2), ethylene (C_2H_4), and ethane (C_2H_6) concentrations are shown. The model overpredicted the methane concentration in the 0.15-0.25cm region of the main reaction zone by a factor of 1.3 although in the 0.28-0.38cm region the methane profile was well simulated. The model was unable to predict the apparent ca. 50% drop from its peak concentration in the post reaction zone. Methane was primarily formed by $C_2H_4+CH_3 \leftrightarrow C_2H_3+CH_4$ and secondarily by $CH_3+H_2 \leftrightarrow CH_4+H$. The overall ethane profile was well simulated by the detailed chemical kinetic model. Ethane is formed by $CH_3+CH_3(+M) \leftrightarrow C_2H_6(+M)$, and is

consumed by $C_2H_6+H \leftrightarrow C_2H_5+H_2$. The ethylene measurements show a somewhat flat profile for the first 0.35 cm of the flame followed by a sharp drop off. The model was unable to predict such a trend and instead showed rapid formation and subsequent consumption of the ethylene occuring in the first 2.5 millimeters of the flame. The ethylene is primarily produced by the reaction sequence $C_4H_{10} \leftrightarrow C_2H_5+C_2H_5$ followed by $C_2H_5(+M) \leftrightarrow C_2H_4+H(+M)$, and is primarily consumed by $C_2H_4+H \leftrightarrow C_2H_3+H_2$. The model well predicted the acetylene concentrations as observed in the experiment, however, good agreement was only obtained when the rate constant assignments for $C_2H_3+O_2 \leftrightarrow CH_2O+HCO$, $C_2H_3+O_2 \leftrightarrow CH_2CHO+O$ were altered from those used in our previous modeling work [11]. The newly assigned rate constants may be found in Table 1 and were taken from our earlier work on ethylene oxidation [64]. These particular rate expressions were based on the privately communicated QRRK calculation of Westmoreland [64] for the $C_2H_3+O_2$ reaction system. An adjustment was made to the rate constant A-factor for $C_2H_3+O_2 \leftrightarrow CH_2HCO+O$ so as to obtain agreement with our earlier well-stirred reactor ethylene oxidation experiments. The acetylene formation reaction, $C_2H_3+O_2 \leftrightarrow C_2H_2+HO_2$, that occurs through the chemically activated $C_2H_3O_2$* adduct, was removed from the model since the $C_2H_3+O_2$ metathesis reaction is able to reproduce the acetylene concentrations seen in our earlier ethylene oxidation work as well as the present work. Reaction flux analysis indicated that acetylene formation in the region near the burner surface (e.g., from 0.0cm to 0.20cm) was primarily controlled by $C_2H_3+O_2 \leftrightarrow C_2H_2+HO_2$ and secondarily by $C_2H_3(+M) \leftrightarrow C_2H_2+H(+M)$ and $pC_3H_4+H \leftrightarrow C_2H_2+CH_3$. In the downstream region from 0.20cm above the burner surface to the end of the computational domain, $C_2H_3(+M) \leftrightarrow C_2H_2+H(+M)$ was the primary acetylene production pathway followed by a secondary amount of acetylene produced by the metathesis reaction, $C_2H_3+O_2 \leftrightarrow C_2H_2+HO_2$.

In figure 2(b), the measured and predicted C_3H_4 (C_3H_4 is the sum of aC_3H_4(allene) and pC_3H_4(propyne)), diacetylene (C_4H_2), and C_4H_4 (C_4H_4 is the sum

of CH_2CHCCH and H_2CCCCH_2) concentrations are shown. The C_3H_4 concentration was fairly well predicted across the n-butane flame, although the model was unable to reproduce the peak location of the C_3H_4 concentration occurring around 0.35cm. The C_3H_4 was produced by the reaction sequence of $C_4H_{10}+H \leftrightarrow sC_4H_9+H_2$, $sC_4H_9(+M) \leftrightarrow C_3H_6+CH_3(+M)$, $C_3H_6+H \leftrightarrow aC_3H_5+H_2$, $aC_3H_5+H \leftrightarrow aC_3H_4+H_2$, and $aC_3H_4 \leftrightarrow pC_3H_4$ as shown in figure 3. Propene was not detected in this flame, however the model predicted a peak C_3H_6 concentration of ca. 0.9% at 0.12cm above the burner surface followed by a quick decay to 13ppm at 0.50cm in the post-reaction zone. The diacetylene (C_4H_2) concentrations were underpredicted by approximately one order of magnitude throughout the flame. We have similarily underpredicted the diacetylene concentrations by one order of magnitude in our earlier flame modeling studies of methane, ethane, ethylene, and propane. Effort was made in trying to improve the predicted diacetylene concentration in this study, but we were unable to model the diacetylene measured in this flame without greatly overpredicting the diacetylene measured in the rich, premixed, ethylene flames of Harris [7], and the rich, premixed, acetylene flame of Bastin [8]. The diacetylene was predicted to be formed primarily by $C_2H+C_2H_2 \leftrightarrow C_4H_2+H$ and secondarily by vinyl acetylene dehydrogenation. The experiments showed that the C_4H_4 concentration peaked around 0.35cm above the burner surface then decays in the post-reaction zone. The model predicted the peak concentration of vinylacetylene occurs earlier, around 0.20cm, then slowly decays in the post-reaction zone. The C_4H_4 concentration was well reproduced only from 0.15-0.20cm and underpredicted in the post-reaction zone by a factor of 2 to 4. The $C_2H_3+C_2H_2 \leftrightarrow CH_2CHCCH+H$ reaction was the primary route to CH_2CHCCH formation in the n-butane flame, while $CH_2CHCCH+H \leftrightarrow H_2CCCCH+H_2$ was the primary C_4H_4 consumption step.

A summary of the low molecular weight aliphatics and combustion by-products formation pathways is shown in figure 3. The thickness of the arrow represents the relative importance of the reaction pathways in the overall n-butane rich oxidation scheme. These

reaction pathways serve as the underlying foundation for aromatic, polycyclic aromatic hydrocarbon (PAHs) and potentially soot growth in flames. The principal pathway to the formation of aromatic precursors in the n-butane flame is represented by the sequence I pathway. This pathway is described by abstraction by H-atom from n-butane to form the iso-butyl (sC_4H_9) radical followed by decomposition to propene and methyl. The propene is primarily dehydrogenated by H-atoms and leads to the production of resonantly stabilized allyl and propargyl radicals. These radicals are instrumental to the formation of aromatics in this flame. The sequence II pathway represents how many of the low molecular weight aliphatics and major combustion by-products are formed. The n-butane decomposes to n-butyl (pC_4H_9), n-propyl, methyl, and ethyl radicals whereupon the nbutyl, n-propyl, and ethyl radicals are primarily removed from the flame by pC_4H_9(n-butyl)(+M)$\leftrightarrow C_2H_5+C_2H_4$(+M), nC_3H_7(+M)$\leftrightarrow C_2H_4+CH_3$(+M), C_2H_5(+M)$\leftrightarrow C_2H_4+H$(+M). Ethylene and methane were the primary hydrocarbon products experimentally observed in the early oxidation stage of the n-butane flame as confirmed by the model. The ethylene conversion to products is complicated by the multiple destruction routes involving the vinyl radical as shown in figure 3.

Formation Pathways of Aromatics, Branched Aromatics, and PAHs

In this section, we present a road map of how n-butane reacts and leads to the formation of aromatic and PAH precursor species, aromatics, and PAH's. The reaction flux analysis for the production and destruction of aromatics and PAH's are essentially controlled by reactions involving the combination of resonantly stabilized radicals, ring destruction by O_2, PAH isomerization, and acetylene addition to benzylic radicals. The importance of these reactions may be summarized by the flow diagrams shown in figures 3, 4, and 5. The flow diagrams represent the reaction flux analysis of the detailed chemical kinetic model and identifies the chemical pathways that are believed to be important to aromatic,

branched aromatic, and polycyclic aromatic hydrocarbon growth and removal in aliphatic flames.

Figures 4 and 5 illustrates the important chemical pathways that lead to the production of aromatics and polycyclic aromatic hydrocarbons in the n-butane flame. The first step is forming the aromatic ring (steps 1(b) and 1(e)) via resonantly stabilized propargyl and allyl radicals then activating it by abstracting an H-atom (step 1(c)) to form the phenyl radical or forming phenyl directly from propargyl recombination (step 1(b)). The phenyl is oxidized by O_2 to form a phenoxy radical which unimolecularly decomposes to cyclopentadienyl and CO. This is noted by steps 2 and 3. The resonantly stabilized cyclopentadienyl radical then self-combines to form naphthalene as shown in step 4 [11, 57, 65-68]. The naphthalene must be activated by H-atom abstraction by H-atom to form naphthyl ($C_{10}H_7$) which is then subsequently oxidized by O_2 to form a naphthoxy radical followed by unimolecular decomposition to indenyl and CO as noted by steps 5, 6, and 7. The resonantly stabilized indenyl species can combine with a cyclopentadienyl moiety to form the 3-fused aromatic ring phenanthrene as shown in step 8 [11]. Anthracene formation occurs by isomerization from phenanthrene [69]. The most important steps involved in this PAH formation process requires the phenyl (C_6H_5) and naphthyl ($C_{10}H_7$) to be oxidized by O_2 (steps 2 and 6). This oxidation process plays an important role in the PAH growth process under fairly fuel-rich oxidation conditions as well as serving as an important aromatic and PAH destruction route under fuel-lean oxidation conditions. Our modeling results have shown that PAH formation is promoted by small amounts of O_2 rather than inhibited as previously believed based on the hydrogen abstraction - acetylene addition (HACA) mechallism. This is shown as steps 10 and 11 in figure 4.

Figure 5 illustrates the importance of the acetylene addition to benzylic radicals to PAH formation. The benzyl radical is formed in step 12 by the combination of propargyl and 1-methylallenyl radicals. The benzyl radical can combine with an H-atom to form

toluene become oxidized by HO_2, OH, or O-atoms to form benzene. The acetylene addition to a benzyl radical leads to the formation of a cyclic C_5 structure fused to an aromatic ring (e.g., indene, benz[a]indene) as shown in step 13. This step is important to the formation of high molecular weight growth compounds in flames, especially in absence of sufficient O_2 to oxidize the naphthyl radical as shown in steps 6 an 7 in figure 4. The hydrogens found on the sp^3 carbon in the 5-membered ring moeity are very weak and therefore can be easily abstracted (step 14). The bond dissociation energy for these indylic C-H bonds is typically 75.0kcal/mol - 79.0kcal/mol [20,70]. Once the H-atom is abstracted, these indenyl-type compounds can combine with species having the cyclopentadienyl moiety and form larger polycyclic aromatic hydrocarbons (step 8).

Cyclics, Aromatics, and Polycyclic Aromatics - Modeling Results and Sensitivity Analysis

Benzene The propargyl-propargyl self-combination reaction accounted for approximately 80% of the benzene formed in this flame with the remaining contribution due to the reaction sequence $aC_3H_5+H_2CCCH \leftrightarrow$Fulvene+H followed by conversion of fulvene to benzene by H-atom catalysis, Fulvene+H$\leftrightarrow$Benzene+H. The model was able to reproduce the experimental benzene profile fairly well for distances greater than 0.15cm above the burner surface (figure 6(a)). The sharp rise in benzene formation is attributed to the rapid production of aromatic precursor species from the decomposed butane fuel as noted in sequence 1 of figure 3. The predicted benzene concentration levels off in the vicinity of the peak temperature and slowly rises in the post-reaction zone. The leveling off in the benzene profile is attributed to the H-atom pool (see figure 11) which consumes propargyl and benzene by H-atom abstraction reactions thereby limiting the growth of benzene.

Normalized sensitivity coefficients were calculated for propargyl and benzene as shown in figures 7(a) and 7(b), respectively. A positive sensitivity coefficient value implies that the reaction enhances the species production rate or slows its destruction rate, while a

negative sensitivity coefficient implies the opposite. The sensitivity analysis results indicates that propargyl and benzene production are very sensitive to the H-atom abstraction reactions of sequence 1 as shown by the reaction flux analysis diagram of figure 4. The rate coefficient choices for $aC_3H_5+H \leftrightarrow aC_3H_4+H_2$, $aC_3H_4+H \leftrightarrow H_2CCCH+H_2$, $aC_3H_4+H \leftrightarrow H_2CCCH+H_2$, and $H_2CCCH+H \leftrightarrow C_3H_2+H_2$ are very important to aromatic ring growth in the main reaction zone as exhibited by the sensitivity analysis results. Unfortunately, there is no experimental kinetic rate data for these H-atom abstraction reactions that could give some indication to the accuracy of rate constants used in the present model. We have chosen to use the rate constants for these reactions as advocated by Miller [30] and Tsang [32]. The $H_2CCCH+H \leftrightarrow C_3H_2+H_2$ and $C_6H_6+H \leftrightarrow C_6H_5+H_2$ reactions, and phenyl oxidation by O_2 to produce phenoxy (C_6H_5O) and O-atom were determined to be important steps which limits the net production of benzene (Fig. 7(b)). Interestingly, although the $H+O_2 \leftrightarrow OH+O$ reaction exhibited secondary sensitivity to propargyl production in main reaction zone, it exhibits extraordinary sensivity to benzene production in the post-reaction zone. This result, although at first glance may seem a bit peculiar, is explained by noting that $H+O_2 \leftrightarrow OH+O$ consumes those species (i.e., H-atom and O_2) which would otherwise contribute to the destruction of benzene and phenyl (i.e., $C_6H_6+H \leftrightarrow C_6H_5+H_2$ and $C_6H_5+O_2 \leftrightarrow C_6H_5O+O$).

Cyclopentadiene The predicted profile for cyclopentadiene is shown in Fig. 6. The predicted peak concentration (ca. 27ppm) underpredicts the measured peak by approximately a factor of 2.5. As discussed later, the model predicts a significant peak concentration of cyclopentadienyl radical of ca. 23 ppm. If these radicals combine with H-atoms in the sampling line, the measured cyclopentadiene concentration would be representative of the sum of the radical and the parent. This sum predicted by the model is shown also shown in Fig. 6 and compares quite well with the measured cyclopentadiene

concentration for the first 0.30 cm of the flame. The model indicates that the peak cyclopentadiene concentration should occur around 0.25cm which differs from the experimental measurement determination of 0.35cm. The situation where the daughter radical species concentration is of the same order of concentration as the parent stable species occurs only for the parent-daughter pairing of indene and indenyl. Those species will be discussed later. The same approach of adding the parent concentration to the daughter is used in this case as well. Reaction flux analysis shows that cyclopentadiene is primarily formed by the reaction sequence of $C_6H_5+O_2 \leftrightarrow C_6H_5O+O$, $C_6H_5O \leftrightarrow c\text{-}C_5H_5+CO$, and $c\text{-}C_5H_5+H \leftrightarrow c\text{-}C_5H_6$. Sensitivity analysis was applied to the cyclopentadienyl ($c\text{-}C_5H_5$) radical due to its importance in the naphthalene production process as advocated by our earlier work [11].

The normalized sensitivity coefficients for cyclopentadienyl are shown in figure 8(a). The greatest sensitivities are exhibited in the main reaction zone region where the cyclopentadienyl radical accumulates in concentration due to the reaction sequence of $C_6H_5+O_2 \leftrightarrow C_6H_5O+O$ followed by $C_6H_5O \leftrightarrow c\text{-}C_5H_5+CO$. The large negative sensitivity coefficient exhibited by $c\text{-}C_5H_6+H \leftrightarrow aC_3H_5+C_2H_2$ indicates the importance this reaction has in consuming cyclopentadiene. The $C_2H_3(+M) \leftrightarrow C_2H_2+H(+M)$, $C_2H_3+CH_3 \leftrightarrow aC_3H_5+H$, and $HCCO+O_2 \leftrightarrow HCO+CO+O$ reactions exhibit negative sensitivity coefficients primarily due to their ability to produce H-atoms which consumes $c\text{-}C_5H_6$ in the main and post reaction zones. The $H_2CCCH+H \leftrightarrow C_3H_2+H_2$ reaction exhibits a negative sensitivity coefficient since this reaction consumes propargyl radicals which prevents benzene/phenyl formation hence cyclopentadiene from forming in the flame. The methyl radical recombination reaction exhibits a positive sensitivity coefficient since this reaction removes methyl radicals from the flame which limits propargyl consumption by $H_2CCCH+CH_3 \leftrightarrow$ Products.

Interestingly, the $aC_3H_5+C_2H_2 \leftrightarrow c\text{-}C_5H_6+H$ reaction shows a slight positive sensitivity coefficient near the burner surface before the reaction reverses in direction and

shows a very large negative sensitivity coefficient in the post-reaction zone. The positive sensitivity coefficient is due to the relatively large amounts of allyl and acetylene produced near the burner surface. These large concentrations of allyl and acetylene enables this forward reaction to overcome the ca. 15-20 kcal/mol thermodynamic barrier in the gibbs free energy change (ΔG, where $\Delta G = -RT\ln K_{eqlbrm}$) for the 1100K-1300K temperature range so as to produce cyclopentadiene. The reaction reverses in direction as the cyclopentadiene and H-atom concentrations increase in the later stages of the main reaction and post-reaction zones.

Naphthalene The key step in the naphthalene production process is phenyl oxidation by O_2. This step produces a phenoxy radical which decomposes to c-C_5H_5+CO. The cyclopentadienyl radicals self-combine, and then undergo H-atom shifts and two H-atom ejections leading to naphthalene production. Melius [57] has discussed the reaction mechanism for the self-combination of cyclopentadienyl radicals leading to naphthalene and H-atoms formation. We have assigned a global rate constant of 2.00E+13 Exp(-8000cal/mol/RT) for this reaction based on the assumption that the rate limiting step for this reaction is the 8.0±5.0kcal/mol intrinsic barrier height [57] attributed to the ejection of the first H-atom from the bicyclopentadienyl adduct. The 1,5-hydrogen shifts in the bicyclopentadienyl adduct occur fairly rapidly with intrinsic activation energies of ca. 25.0 kcal/mol [57] which are considerably lower than the ca. 60 koal/mol bond dissociation energy back to reactants. After the ejection of the first H-atom, the 1-hydrofulvalenyl undergoes fairly rapid unimolecular isomerizations to naphthalene+H or H-atom bond scissioning to fulvalene at these flame temperatures. In the former process, 1-hydrofulvalenyl isomerizes through a series of resonant stabilizing ring opening and closing transition states and intermediates on its way to naphthalene+H, and those intermediates are unlikely to be intercepted. The later process of H-atom bond scissioning

to fulvalene+H is fast compared to the channel leading to naphthalene+H. The fulvalene will react with H-atom and undergo rearrangement to napthalene+H fairly exothermically.

The measured and predicted naphthalene concentration is shown in figure 6(a). The model well simulated the naphthalene concentration profile for distances greater than 0.20cm where the agreement was within 20%. The model was unable to correctly predict the rapid naphthalene formation that occurred near the burner surface. The slow down in the predicted net naphthalene production rate in the post-flame zone is caused by the reduced net cyclopentadienyl production rate, and naphthalene consumption by H-atoms in making naphthyl ($C_{10}H_7$) which is subsequently oxidized by O_2. Naphthalene normalized sensitivity coefficients were calculated as shown in figure 8(b). The results indicate that the removal of cyclopentadiene and propargyl radical by H-atoms inhibits naphthalene production, while reactions which can increase cyclopentadienyl formation (e.g., $C_6H_5+O_2 \leftrightarrow C_6H_5O+O$) enhance naphthalene production. The vinyl and formyl radical decomposition reactions exhibit a negative sensitivity coefficient since these reactions provide a source of H-atoms which helps to consume propargyl (e.g., $H_2CCCH+H \leftrightarrow C_3H_2+H_2$) and cyclopentadiene (e.g., $c\text{-}C_5H_6+H \leftrightarrow aC_3H_5+C_2H_2$) and thus inhibit naphthalene formation.

Toluene, Ethyl Benzene, Styrene, and Phenyl Acetylene The measured and predicted concentrations of toluene, ethyl benzene, o-xylene, styrene, and phenyl acetylene are shown in figure 6(b). The toluene ($C_6H_5CH_3$) measurements show a gradual rise and fall in the concentration profile with the peak concentration occuring around 0.35cm-0.40cm downstream of the burner surface. The model was able to reproduce this trend including the proper prediction of the location for the peak concentration. The model was able to predict the toluene concentration to within a factor of two for the 0.15cm to 0.45cm region of the flame. Toluene formation occurs by the reaction sequence $CH_3CCCH_2+H_2CCCH \leftrightarrow C_6H_5CH_2(benzyl)+H$ and $C_6H_5CH_2+H \leftrightarrow C_6H_5CH_3$. The resonantly

stabilized 1-methylallenyl (CH_3CCCH_2) and propargyl (H_2CCCH) radicals react in an analogous manner as to the propargyl recombination reaction, and this leads to toluene formation without having to form benzene first. The rate constant assigned to $CH_3CCCH_2+H_2CCCH \leftrightarrow C_6H_5CH_2+H$ was assumed to be of similar value as to $H_2CCCH+H_2CCCH \leftrightarrow C_6H_5+H$. The ethyl benzene ($C_6H_5C_2H_5$) peak concentration location was predicted by the model to occur around 0.15cm while the experimental data indicates a fairly flat profile from the burner surface to 0.35cm downstream. The model fairly well simulated the measured $C_6H_5C_2H_5$ concentration profile to within a factor of two. Styrene ($C_6H_5C_2H_3$) measurements show a peak concentration of ca. 10ppm occuring around 0.35cm while the model predicted a peak concentration of ca. 5ppm around 0.20cm. The difference between the the model prediction and experimental measurement is most likely attributed to differences shown in the predicted versus measured ethylene profiles for the n-butane flame. The model was able to predict styrene to within a factor of two across the flame and fairly well represented the measured styrene profile. The important styrene formation step in this flame was $C_6H_5+C_2H_4 \leftrightarrow C_6H_5C_2H_3+H$. Phenyl Acetylene ($C_6H_5C_2H$) was underpredicted by approximately a factor of three to four throughout the post-reaction zone with the model indicating styrene dehydrogenation (i.e., $C_6H_5C_2H_3+H \leftrightarrow C_6H_5CCH_2+H_2$, $C_6H_5CCH_2+H \leftrightarrow C_6H_5C_2H+H_2$) as the preferred phenyl acetylene production route. The $C_6H_5+C_2H_2 \leftrightarrow C_6H_5C_2H+H$ pathway, which might be expected to produce phenyl acetylene, was favored in the reverse direction and served as the primary phenyl acetylene removal step. We have examined the heat of formation assignments for C_6H_5 and $C_6H_5C_2H$ and adjusted those values within the limits permitted by the thermodynamics literature base so as to assess the sensitivity of the phenyl acetylene prediction to these parameters. The closest agreement to the phenyl acetylene measurements occurred when using a heat of formation value of 82kcal/mol for C_6H_5 [71] and the group additivity calculated value of 73.9kcal/mol for $C_6H_5C_2H$ [11]. However, this heat of formation

choice for C_6H_5 did not significantly improve the phenyl acetylene prediction. The phenyl acetylene heat of formation as used in this study is low compared to the experimentally determined value of 78.22kcal/mol [72]. If we had used this value then we would have obtained a slightly poorer phenyl acetylene prediction. Similiar underpredicted phenyl acetylene concentrations have been shown in our previous modeling works, and we must conclude that there must exist another phenyl acetylene production route other than the styrene dehydrogenation reaction sequence to phenyl acetylene as found in the current model.

Phenanthrene, Anthracene, Acenaphthylene, and Pyrene The measured and predicted concentrations of these species are shown in figure 9(a). The phenanthrene ($C_{14}H_{10}$) formation trend was fairly well predicted by the model in the post-reaction zone. The experimental measurements indicated phenanthrene forming in larger abundance nearer the burner surface than predicted by the model. Therefore, further work is needed to establish the phenanthrene formation mechanism. Sensitivity and reaction flux analysis indicated Indenyl+c-C_5H_5↔Phenanthrene+H+H in the pre-reaction zone of the flame was the important phenanthrene formation step. Anthracene ($C_{14}H_{10}$) formation is thought to occur by the isomerization of phenanthrene as previously suggested by Colket and Seery [68] and our earlier modeling studies. The model well predicted the experimental anthracene concentration in the main and post-reaction zones which strongly supports the findings of Colket and Seery. Acenaphthylene ($C_{12}H_{10}$) was consistently underpredicted by a factor of 10 throughout the n-butane flame when using $C_{10}H_7+C_2H_2$↔Acenaphthylene+H as the acenaphthylene formation step. In our previous modeling efforts with methane, ethane, ethylene, and propane flames, we were able to obtain agreement with the acenaphylene profile to within a factor of 2.5 to 20 although in all cases we underpredicted the acenaphthylene concentrations. We must conclude that other alternative acenaphthylene formation mechanisms, other than the commonly accepted

$C_{10}H_7+C_2H_2 \leftrightarrow$ Acenaphthylene+H reaction, must exist in flames. These presently unknown acenaphthylene formation routes account for the remaining difference between the model prediction and the experimental measurement. The pyrene concentration profile was underpredicted by approximately an order of magnitude in the post-reaction zone when using the reaction step of Phenanthryl-4+$C_2H_2 \leftrightarrow$ Pyrene+H at its upper limit rate expression [11] as obtained from Wang and Frenklach [35]. The underprediction of the pyrene found in this study and in our previous modeling studies seems to indicate that another pyrene formation route exists.

O-Xylene, Indene, Biphenyl, and Fluoranthene The measured and predicted concentrations of o-xylene, indene, biphenyl and fluoranthene are shown in figure 9(b). The experimentally observed o-xylene concentrations were shown to be fairly well predicted in the region near the burner surface to approximately 0.35cm. The model indicated a peak concentration of o-xylene occurred around 0.15cm while experimental measurements indicated a flat concentration profile. The model overpredicted the o-xylene concentration by a factor of 5 to 10 in the post-reaction zone. The o-xylene production sequence as found in the model is 1-methylallenyl (CH_3CCCH_2) self combination to form o-xylyl ($CH_3C_6H_4CH_2$)+H, followed by o-xylyl combination with H-atom to make o-xylene. The model predicts that the peak concentrations of the parent species indene and the daughter radical indenyl are of the same order of magnitude. This is the same situation as seen earlier for the parent species cyclopentadiene. The indene (C_9H_8) experimental concentration profiles may be modeled fairly well when considering the predicted sum of indene and indenyl concentrations. It is not clear what fraction of the indenyl will be converted to indene or become lost in the gas sampling line, but the summed concentration from the model does a fair job in predicting the indene profile across the main and postreaction zones of the n-butane flame. Indene's formation pathway occurs by either the reaction step $C_6H_5CH_2+C_2H_2 \leftrightarrow$ Indene+H or by the reaction sequence

$C_{10}H_8+H \leftrightarrow C_{10}H_7+H_2$, $C_{10}H_7+O_2 \leftrightarrow C_{10}H_7O+O$, $C_{10}H_7O \leftrightarrow$ Indenyl+CO, Indenyl+H$\leftrightarrow$Indene. The experimental biphenyl ($C_{12}H_{10}$) concentration profile was consistently underpredicted by a factor of two. However, the profile was fairly well simulated when using only the biphenyl formation steps of $C_6H_5+C_6H_5 \leftrightarrow$ Biphenyl and $C_6H_5+C_6H_6 \leftrightarrow$ Biphenyl+H, and the destruction step of Biphenyl+H$\leftrightarrow C_6H_5+C_6H_6$. Fluoranthene ($C_{16}H_{10}$) was poorly predicted when using the reaction steps of $C_6H_5+C_{10}H_7 \leftrightarrow$ Fluoranthene+H+H and $C_6H_6+C_{10}H_7 \leftrightarrow$ Fluoranthene+H_2+H in the model. The model underpredicted the experimental fluoranthene concentration by approximately two to three orders of magnitude and again supports our earlier claim [11,12] that another mechanism leading to fluoranthene formation is operative. Further work is needed to understand the formation mechanisms of PAHs that have a C_5 structure sandwiched around aromatic rings (e.g., fluoranthene, 9h-fluorene etc.).

9H-Fluorene, Benzo(ghi)fluoranthene, c-Penta(cd)pyrene, and 4H-cyclopenta(def)phenanthrene The measured and predicted concentrations of these species are shown in figure 10(a). Modeling was not performed for c-penta(cd)pyrene and we have included the experimental data as shown in the figure. The 9h-fluorene profile was well predicted by the model for the later stages of the main and post reaction zones of the n-butane flame. This result suggests that the reaction sequence of Phenanthryl-9 +O2$\leftrightarrow$Phenanthroxy-9+O, Phenanthroxy-9$\leftrightarrow$Fluoryl+CO, and Fluoryl+H$\leftrightarrow$9H-Fluorene may produce the necessary 9h-fluorene concentrations as observed in the experiment. Further research is needed to verify the rate constants chosen in this reaction sequence. Benzo(ghi)fluoranthene and cyclopenta(cd)pyrene are 5 fused aromatic ring PAHs that exhibit a rapid increase in concentration within the main to post-reaction zones. The model has not been properly developed to treat the formation and destruction of these particular species, however we do show the modeling results for benzo(ghi)fluoranthene. Further work is needed to understand the formation mechanisms of those species that have 5 fused

aromatic rings. The 4H-cyclopenta(def)phenanthrene profile was well predicted by the model for the later stages of the main and post reaction zones. This result suggests that the reaction sequence of $CH_3CCCH_2+CH_3CCCH_2 \leftrightarrow$ O-Xylyl+H, O-Xylyl+$C_2H_2 \leftrightarrow$ Methylindene(CH_3indene)+H, Methylindene+H$\leftrightarrow$Methylindenyl+H_2, Methylindenyl+c-$C_5H_5 \leftrightarrow$Methylphenanthrene(CH_3phenanthrene)+H, and Methylphenanthrene+H$\leftrightarrow$4H-cyclopenta(def)phenanthrene+H2+H, may produce the necessary 4H-cyclopenta(def)phenanthrene concentrations as observed in the experiment. Further research is needed to verify the rate constants chosen in this reaction sequence.

Azulene, Biphenylene, 1-HPhenalene, and Benzo(a)pyrene The current model was not developed to predict these species which are detected in the n-butane flame. We have included the data for these molecules as shown in figure 10(b) as part of the complete data set for this flame. The structural features and relative stabilities of these species are found in Castaldi (1995). The azulene ($C_{10}H_8$) measurements exhibit a rolling profile with a peak concentration of ca. 1.4 ppm around 0.4 cm. The biphenylene ($C_{12}H_8$) concentration profile showed a rapid rise in the later stages of the main reaction zone and then leveled out in the post-reaction zone with a concentration of ca. 0.60 ppm. 1-HPhenalene ($C_{13}H_{10}$) exhibited a fairly flat profile from the later stages of the main reaction zone to the post-reaction zone of the n-butane flame. Benzo(a)pyrene ($C_{20}H_{12}$) is a 5 fused aromatic ring species whose concentration was measured in the post reaction zone with a maximum value of 2.9E-2ppm at 0.6 cm.

Predicted Radical Concentrations for the n-Butane Flame The predicted H-atom, CH_3, C_2H_3, H_2CCCH, aC_3H_5, i-C_3H_7 (CH_3CHCH_3), n-C_3H_7 ($CH_3CH_2CH_2$), H_2CCCCH, CH_3CCCH_2, CH_2CHCCH_2, c-C_5H_5, C_6H_5, C_6H_5O, $C_6H_5CH_2$, and Indenyl (C_9H_7) radical concentrations for the n-butane-oxygen-argon burner stabilized flame are shown in figures 11(a), 11(b), and 12.

The relative ranking of the major C_1-C_3 radical concentrations and H-atom from the burner surface to ca. 0.15cm is CH_3>aC_3H_5>H_2CCCH≥C_2H_3 and for distances greater than 0.25cm the ranking becomes CH_3>H_2CCCH>aC_3H_5≈H>>C_2H_3. It is interesting note that the free radical in the highest concentration is not H-atoms but methyl radicals. The methyl radical concentration was also the largest in the previously investigated methane [11], ethane [11], and propane flames [13]. The methyl radicals are in abundance because they are difficult oxidize under fairly rich oxidation conditions. The allyl and methyl radicals exhibited similiar concentration profiles for the first 1.5 millimeters, but the allyl radical profile decays rapidly in the post-reaction zone as it becomes consumed by H-atoms. The propargyl radical concentration does not decay as fast as allyl since propargyl formation benefits from allyl dehydrogenation through reaction sequence, aC_3H_5+H↔aC_3H_4+H_2, aC_3H_4+H↔H_2CCCH+H_2, aC_3H_4↔pC_3H_4 and pC_3H_4+H↔H_2CCCH+H_2. The vinyl radical (C_2H_3) exhibits a much lower concentration in the flame than allyl and propargyl as vinyl is more reactive, especially with molecular oxygen.

The relative ranking of the major C_4 radical concentrations from the burner surface to the first 0.25cm is very complicated. The C_4H_5 isomers (CH_3CCCH_2 and CH_2CHCCH_2) and C_4H_7 dominate in the burner surface to 0.14cm region of the flame. The allylic resonant stabilized C_4H_7 (methylallyl) radical is formed by the reaction sequence of aC_3H_5+CH_3↔C_4H_8-1 and C_4H_8-1+H ↔C_4H_7+H_2. The C_4H_7 radical production decays rapidly for distances greater than 0.15cm due to the reversibility at higher temperatures associated with aC_3H_5+CH_3↔C_4H_8-1 and C_4H_7 decomposition to 1,3-butadiene. The CH_2CHCCH_2 (i-C_4H_5) radical dominates near the burner surface but decays rapidly in the post-reaction zone as the higher temperatures found in this region accelerate decomposition to CH_2CHCCH (vinyl acetylene) and H-atom. In the post-reaction zone, CH_2CHCCH_2 is also removed by H-atoms to give propargyl and methyl radical. The CH_2CHCCH_2 is formed near the burner surface primarily by the reaction

seqeunce of allyl and methyl combination leading to C_4H_8-1 followed by C_4H_8-1 dehydrogenation to CH_2CHCCH_2. In the post-reaction zone, the relative ranking of these radicals are CH_3CCCH_2>H_2CCCCH>CH_2CHCCH_2>>C_4H_7. The CH_3CCCH_2 is formed in greater abundance than the other C_4 radicals in the post-reaction zone due primarily to the conversion of propargyl to a methylated propargyl by methyl radicals. The resonantly stabilized H_2CCCCH radical is formed via $C_2H_3+C_2H_2 \leftrightarrow CH_2CHCCH+H$ followed $CH_2CHCCH+H \leftrightarrow H_2CCCCH+H_2$.

Representative predictions for cyclopentadienyl (c-C_5H_5), phenyl (C_6H_5), phenoxy (C_6H_5O), benzyl ($C_6H_5CH_2$), and indenyl (C_9H_7) are shown in figure 12. The phenoxy concentration is slightly higher and peaks earlier than phenyl due to the rapid removal of phenyl by the O_2 in the main reaction zone. As the O_2 becomes depleted, phenyl is no longer quickly removed by O_2 so that the phenoxy concentration decays rapidly. The benzyl radical concentration increases rapidly in the main reaction and early post-reaction zones due to the rapid formation from the combination reaction of 1-methylallenyl and propargyl radicals. The benzyl is consumed by reactions involving H-atoms, $C_6H_5CH_2+H \leftrightarrow C_6H_5CH_3$, and HO_2 radicals, $C_6H_5CH_2+HO_2 \leftrightarrow C_6H_5CHO+OH+H$. The resonantly stabilized indenyl and cyclopentadienyl radicals do not decay as fast and are predicted to be formed in greater abundance than phenyl, phenoxy, and benzyl which allows these species to be potential precursors for high molecular weight PAH production.

Summary

An experimental and modeling study has been performed to investigate aromatic and polycyclic aromatic hydrocarbon formation pathways in a rich, sooting, n-butaneoxygen argon burner stabilized flame. The experiment was conducted using an atmospheric pressure laminar flat flame operated at an equivalence ratio of 2.6. Microprobe gas

sampling coupled with an on-line gas chromatograph/mass spectrometer (GC/MS) system was used in undertaking the spatially resolved species measurements. Data was collected in the main reaction and post-reaction zones for a number of low molecular weight species, aliphatics, aromatics, and polycyclic aromatic hydrocarbons (PAHs) ranging from two to five-aromatic fused rings.

A previously developed detailed chemical kinetic model for rich, premixed, methane, ethane, ethylene and propane flames was used to interpret the experimental measurements derived from the premixed n-butane flame. Reaction flux and sensitivity analysis were used to help identify the important reaction sequences leading to aromatic and polycyclic aromatic hydrocarbon growth and destruction. Reaction flux analysis showed the production and destruction of aromatics and PAH's were essentially controlled by reactions involving the combination of resonantly stabilized radicals, ring destruction by O_2, PAH isomerization, and acetylene addition to benzylic radicals.

Propargyl recombination, $H_2CCCH+H_2CCCH \leftrightarrow C_6H_6$ (Benzene), formed most of the benzene in the n-butane flame with secondary contribution from the allyl and propargyl combination reaction to make fulvene, $aC_3H_5+H_2CCCH \leftrightarrow$ Fulvene+H+H, followed by fulvene conversion to benzene by H-atom catalysis, Fulvene+H$\leftrightarrow$Benzene+H. The allyl and propargyl radicals that lead to benzene formation were produced from the reaction sequence of $C_4H_{10}+H \leftrightarrow sC_4H_9+H_2$, $sC_4H_9(+M) \leftrightarrow C_3H_6+CH_3(+M)$, $C_3H_6+H \leftrightarrow aC_3H_5+H_2$, $aC_3H_5+H \leftrightarrow aC_3H_4+H_2$, $aC_3H_4 \leftrightarrow pC_3H_4$, $aC_3H_4+H \leftrightarrow H_2CCCH+H_2$, and $pC_3H_4+H \leftrightarrow H_2CCCH+H_2$. Sensitivity analysis showed the $H_2CCCH+H \leftrightarrow C_3H_2+H_2$ reaction exhibited large negative sensitivity coefficients for propargyl, benzene, and naphthalene. This result implicates propargyl consumption by H-atoms as an important reaction step that limits aromatic and polycyclic aromatic hydrocarbon growth.

The oxidation of phenyl and naphthyl radicals by O_2 exhibited large sensitivity coefficients and these reactions play an important role in the PAH growth and destruction

processes under fuel-rich oxidation conditions. The removal of phenyl and naphthyl by O_2 lead to the eventual formation of PAH precursors, cyclopentadienyl and indenyl, in the n-butane flame. These radicals combine with each other leading to the plausible production of products such as the two fused-aromatic ring, naphthalene, and the three fused-aromatic ring phenanthrene. The modeling results have shown that PAH formation may be promoted by small amounts of O_2 rather than inhibited as previously believed based on the hydrogen abstraction - acetylene addition (HACA) mechanism.

The model was able to predict fairly well the concentrations of benzene, naphthalene, phenanthrene, anthracene, toluene, ethyl benzene, styrene, o-xylene, indene, and biphenyl. The model was unable to simulate properly the concentration profiles of phenyl acetylene, fluoranthene, and pyrene. We attribute the underprediction of these species due to our lack of understanding of the dominant formation mechanisms that produce these species. Since we have not yet included a soot model in the chemical kinetic modeling effort for PAHs such a model could modify those species concentrations. However whether better agreement can be attained by the inclusion of a soot model still remains in doubt. Additional work is needed in furthering our understanding of these complex formation mechanisms.

Acknowledgement

We are most indebted to Wing Tsang for the technical discussions concerning this research and Lila Chase for the computational support in the modeling analysis. The experimental work was supported by the Petroleum Environmental Research Forum Project 92-19 and the U.S. Department of Education. The modeling work was supported by the U.S. Department of Energy, Office of Industrial Technology and performed under the auspices of the U.S. Department of Energy by the Lawrence Livermore National Laboratory under contract No. W-7405-ENG-48.

Figure Captions

Figure 1. Comparison of model predictions with experimental concentration profiles in the n-butane flame. Symbols represent the experimental measurements and the lines represent the model predictions. (a) Comparison to C_4H_{10}, O_2, H_2O and the radiation corrected temperature profile used. (b) Comparison to CO, CO_2, and H_2.

Figure 2. Comparison of model predictions with experimental concentration profiles in the n-butane flame. Symbols represent the experimental measurements and the lines represent the model predictions. (a) Comparison to CH_4, C_2H_2, C_2H_4, and C_2H_6. (b) Comparison to C_3H_4, C_4H_2, and C_4H_4. Numerical computations shown for C_3H_6.

Figure 3. Reaction flux/pathway diagram for the two important reaction sequences leading to reaction intermediates and combustion byproducts that occur in the n-butane-oxygen-argon flame. Species shown in shadowed italics are resonantly stabilized free radicals.

Figure 4. Reaction flux/pathway diagram for the important pathways leading to aromatic and polycyclic aromatic hydrocarbon formation in the n-butane-oxygen-argon flame. Species shown in shadowed italics are resonantly stabilized free radicals.

Figure 5. Reaction flux/pathway diagram for the important pathways leading to aromatic, branched aromatic, and polycyclic aromatic hydrocarbon formation in the n-butane-oxygen-argon flame. Species shown in shawdoed italics are resonantly stabilized free radicals.

Figure 6. Comparison of model predictions with experimental concentration profiles in the n-butane flame. Symbols represent the experimental measurements and the lines represent the model predictions. (a) Comparison to benzene (C_6H_6), naphthalene ($C_{10}H_8$), and cyclopentadiene (c-C_5H_6). (b) Comparison to toluene ($C_6H_5CH_3$), ethylbenzene ($C_6H_5C_2H_5$), styrene ($C_6H_5C_2H_3$), and phenyl acetylene ($C_6H_5C_2H$).

Figure 7. (a) Normalized sensitivity coefficients computed for propargyl (H_2CCCH) and (b) Normalized sensitivity coefficients computed for benzene (C_6H_6) across the n-butane flame.

Figure 8. (a) Normalized sensitivity coefficients computed for cyclopentadienyl (c-C_5H_5) and (b) Normalized sensitivity coefficients computed for naphthalene ($C_{10}H_8$) across the n-butane flame.

Figure 9. Comparison of model predictions with experimental concentration profiles in the n-butane flame. Symbols represent the experimental measurements and the lines represent the model predictions. (a) Comparison to phenanthrene, anthracene, acenaphthalene, and pyrene. (b) Comparison to o-xylene, indene, biphenyl, and fluoranthene. Note: Logarithmic scale used in figures 9(a) and 9(b).

Figure 10. Comparison of model predictions with experimental concentration profiles in the n-butane flame. Symbols represent the experimental measurements and the lines represent the model predictions. (a) Comparison to 9H-fluorene, 4H-cyclopent(def)phenanthrene, and benzo(ghi)fluoranthrene. No comparison is shown for cyclo(cd)pyrene (experimental data only). (b) Experimental concentration profiles (symbols) of Azulene, Biphenylene, 1-HPhenalene, and Benzo(a)pyrene in the n-butane flame. Note: Logarithmic scale used in figures 10(a) and 10(b).

Figure 11. (a) Model prediction of the H, CH_3, C_2H_3, aC_3H_5 and H_2CCCH concentrations in the n-butane flame. (b) Model prediction of the H_2CCCCH, CH_3CCCH_2,CH_2CHCCH_2, and C_4H_7 concentrations in the n-butane flame. Note: Logarithmic scale used in figures 11(a) and 11(b).

Figure 12. Model prediction of the cyclopentadienyl (c-C_5H_5), phenyl (C_6H_5), phenoxy (C_6H_5O), benzyl ($C_6H_5CH_2$), Indenyl (C_9H_7) concentrations in the n-butane flame. Note: Logarithmic scale used in the figure.

References

1. Kirk - Othmer, "Chemical Encyclopedia", 1988.

2. Liss, W. E., Thrasher, W. H., Steinmetz, G. F., Chowdiah, P., and Attari, A. *Variability of Natural Gas Composition in Select Major Metropolitan Areas of the United States*, Gas Research Institute Report No. GRI-92/0123, 1992.

3. Edwards, C. F., and Goix, P. J., *Comb. Sci. Tech.*, In press (1996).

4. Bockhorn, H., Fetting, F., and Wenz, H., *Ber. Bensenges. Phys. Chem.*, 87:1067-1073 (1983).

5. Cole, J.A., Bittner, J.D., Longwell, J.P., and Howard, J.B., *Combust. Flame*, 56:51 (1984).

6. Ciajolo, A., D'Anna, A., Barbella, R., and Tregrossi, A., *Twenty-Fifth Symposium (International) on Combustion*. The Combustion Institute, Pittsburgh, 1994, p. 679.

7. Harris, S.J., Weiner, A.M., Blint, R.J., and Goldsmith, J.E.M., *Twenty-First Symposium (International) on Combustion*, The Combustion Institute, Pittsburgh, 1986, pp. 1033-1045.

8. Harris, S.J., Weiner, A.M., and Blint, R.J., *Combust. Flame*, 72:91 (1988).

9. Bastin, E., Delfau, J.F., Reuillon, M., Volvelle, C., and Warnatz, J., *Twenty-Second Symposium (International) on Combustion*, The Combustion Institute, Pittsburgh, 1988, p. 313.

10. Westmoreland, P.R., Dean, A.M., Howard, J.B., and Longwell, J.P., *J. Phys. Chem.*, 93:8171 (1989).

11. Marinov, N.M., Pitz, W.J., Westbrook, C.K., Castaldi, M.J., and Senkan, S.M., *Combust. Sci. Tech.*, 116-117:211-287 (1996).

12. Castaldi, M.J., Marinov, N.M., Melius, C.F., Senkan, S.M., Pitz, W.J., and Westbrook, C.K.,*Twenty-Sixth Symposium (International) on Combustion.* The Combustion Institute, Pittsburgh, 1996, In press.

13. Marinov, N.M., Castaldi, M.J., Melius, C.F., and Tsang, W. *Combust. Sci. Tech.*, Manuscript submitted.

14. Fitch, W.L., and Sauter, A.D., *Anal. Chem.*, 55:832 (1983).

15. Kee, R.J., Grcar, J.F., Smooke, M.D., and Miller, J.A., "A Fortran Program for Modelling Steady One-Dimensional Premixed Flames. *Sandia Report #SAND85-8240*, Sandia National Laboratories, 1985.

16. Kee, R.J., Rupley, F.M., and Miller, J.A., "CHEMKIN-II: A Fortran Chemical Kinetics Package for the Analysis of Gas Phase Chemical Kinetics. *Sandia Report #SAND 89-8009*, Sandia National Laboratories, 1989.

17. Kee, R.J., Rupley, F.M., and Miller, J.A., "The Chemkin Thermodynamic Database", *Sandia Report #SAND87-8215B*, Sandia National Laboratories, 1987.

18. Burcat, A., and McBride, B., "1994 Ideal Gas Thermodynamic Data for Combustion and Air-Pollution Use",*Technion Report #TAE 697*, 1993.

19. Stein, S.E., and Barton, B.E., *Thermochimica Acta*, 44:265 (1981).

20. Stein, S.E., and Brown, R.L., *J. Am. Chem. Soc.*, 113:787-793 (1991).

21. Benson, S.W., *Thermochemical Kinetics*, Second Edition, John Wiley and Sons, New York, 1976.

22. Stein, S.E., and Fahr, A., *J. Phys. Chem.*, 89:3714 (1985).

23. Cohen, N. and Benson, S.W., *Chem. Rev.*, 93:2419 (1993).

24. Ritter, E.R., and Bozzelli, J.W., *Int. J. Chem. Kinet.*, 23:767-778 (1991).

25. Gordon, S., and McBride, B.J., "Computer Program for Calculation of Complex Chemical equilibrium Compoistions, Rocket Performance, Incident and Reflected Shocks and Chapman-Jouget Detonations", *NASA SP-273* , 1971.

26. Knyazev, V.D., and Slagle, I.R., *J. Phys. Chem.*, 94:2493-2504 (1996).

27. Tsang, W., *J. Phys. Chem.*, 90:1152-1155 (1986).

28. Kee, R.J., Dixon-Lewis, G., Warnatz, J., Coltrin, M.E., and Miller, J.A., "The Chemkin Transport Database", *Sandia Report #SAND86-8246*, Sandia National Laboratories, 1986.

29. Wang, H., and Frenklach, M., *Combust. Flame*, 96:163 (1994).

30. Miller, J.A., and Melius, C.F., *Combust. Flame*, 91:21-39 (1992).

31. Tsang, W., *J. Phys. Chem. Ref. Data*, 17(2):887 (1988).

32. Tsang, W., *J. Phys. Chem. Ref. Data*, 20(2):221 (1991).

33. Pitz, W.J., Westbrook, C.K., and Leppard, W.K.,*SAE Transactions*, SAE Paper No. 912315 (1991).

34. Emdee, J., Brezinsky, K., and Glassman, I., *J. Phys. Chem.*, 96:2151 (1992).

35. Wang, H., and Frenklach, M., *J. Phys. Chem.*, 98:11465 (1994).

36. Towell, G.D., and Martin, J.J., *AICHE J.*, 7:693-698 (1961).

37. Kiefer, J.H., Kapsalis, S.A., Al-Alami, M.Z., and Budach, K.A., *Combust. Flame*, 51:79 (1983).

38. Dean, A.M., *J. Phys. Chem.*, 89:4600 (1985).

39. Baulch, D.L., Cobos, C.J., Cox, R.A., Esser, C., Frank, P., Just, Th., Kerr, J.A., Pilling, M.J., Troe, J., Walker, R.W., and Warnatz, J., *J. Phys. Chem. Ref. Data*, 21:411 (1992).

40. Whytock, D.A., Payne, W.A., and Stief, L.J., *J. Chem. Phys.*, 65:191 (1976).

41. Tsang, W., *Int. J. Chem. Kin.*, 1:245-278 (1969).

42. Allara, D. L., and Shaw, R. A, *J. Phys. Chem. Ref. Data* , 9:523-559 (1980).

43. Walker, R. W., *A Critical Survey of Rate Constants for Reactions in Gas-Phase Hydrocarbon Oxidation, in Reaction Kinetics* (P. G. Ashmore, Ed.), The Chemical Society, Burlington House, London, p. 161, 1975.

44. Yampol'skii, Yu. P., and Nametkin, N.S., *Kinet. Catal.*, 17:57 (1975).

45. Baldwin, R.R., and Walker, R.W., *Trans. Faraday Soc.*, 60:1236-1248 (1964).

46. Azatyan, V.V., *Arm. Khim. Zh.*, 20:577-584 (1967).

47. Yampol'skii, Yu. P., *React. Kinet. Catal. Lett.*, 2:449-452 (1976).

48. Droege, A.T. and Tully, F.P., *J. Phys. Chem.*, 90:5937 (1986).

49. Michael, J. V., Keil, D. G., and Klemm, R. B., *Int. J. Chem. Kin.*, 15:705-719 (1983).

50. Walker, R. W., *Twenty-Second Symposium (International) on Combustion*, The Combustion Institute, Pittsburgh, 1988, pp. 883-892.

51. Sundaram, K. and Froment, G. F., *Ind. Eng. Chem. Fundam.* 17:174-182 (1978).

52. Perry, R. A., *The 8th International Symposium on Gas Kinetics*, 1984.

53. Tully, F. P., *Chem. Phys. Letters*, 143:510 (1988).

54. Smith, G. P., *Int. J. Chem. Kin.*, 19:269 (1987).

55. Edelson, D., and Allara, D. L, *Int. J. Chem. Kinet.*, 12:605-621 (1980).

56. Baldwin, R. R., Bennett, P., and Walker, R. W., *J. C. S. Faraday I*, 76:2396, (1980).

57. Melius, C.F., Colvin, M.E., Marinov, N.M., Pitz, W.J., and Senkan, S.M., *Twenty-Sixth Symposium (International) on Combustion*, The Combustion Institute, Pitssburgh, 1996, In press.

58. Golden, D.M., Gac, N.A., and Benson, S.W., *J. Am. Chem. Soc.*, 91:2136 (1969).

59. Tulloch, J.M., MacPherson, M.T., Morgan, C.A., and Pilling, M.J., *J. Phys. Chem.*, 86:3812 (1982).

60. Jenkin, M.E., Murrells, T.P., Shalliker, S.J., and Hayman, G.D., *J. Chem. Soc. Faraday Trans.*, 89:433-446 (1993).

61. Huntsman, W.D., DeBoer, J.A., and Woosley, M.H., *J. Am. Chem. Soc.*, 88:5846-5850 (1966).

62. Ritter, E.R., Bozzelli, J.W., and Dean, A.M., *J. Phys. Chem.*, 94:2493-2504 (1990).

63. Shandross, R.A., Longwell, J.P., and Howard, J.B., *Twenty-Sixth Symposium (International) on Combustion*, The Combustion Institute, Pittsburgh, 1996, In press.

64. Marinov, N.M., and Malte, P.C., *Int. J. Chem. Kinet.*, 27:957-986 (1995).

65. Manion, J.A., and Louw, R., *J. Phys. Chem.*, 93:3563 (1989).

66. Klinkenberg, W., and Louw, R.,*Thermal Hydrogenolysis of Cyclopentadiene*, CCESRS 87-01, Leiden University: Leiden 1987.

67. Cypres, R., and Bettens, B., *Tetrahedron*, 30:1253 (1974).

68. Cypres, R., and Bettens, B., *Tetrahedron*, 31:359 (1975).

69. Colket, M.B., and Seery, D.J., *Twenty-Fifth Symposium (International) on Combustion.* The Combustion Institute, Pittsburgh, 1994, p. 883.

70. Bordwell, F.G., Cheng, J-P, and Harrelson, J.A., *J. Am. Chem. Soc.*, 110:1229-1231 (1988).

71. Davico, G.E., Bierbaum, V.M., Depuy, C.H., Ellison, G.B., and Squires, R.R., *J. Am. Chem. Soc.*, 117:2590-2599 (1995).

72. Stull, D.E., Westrum Jr., E.F., and Sinke, G.C., *The Chemical Thermodynamics of Organic Compounds,* pp. 401, John Wiley and Sons, 1969.

Table 1: Thermodynamic Properties for Selected Species
Units: kcal/mol for ΔH_f, cal/mol/K for S and C_p

Species	ΔH_f(298K)	S(298K)	C_p(300K)	C_p(400K)	C_p(500K)	C_p(600K)	C_p(800K)	C_p(1000K)	C_p(1500K)
sc4h9†	17.38[a]	79.80[b]	20.93[b]	26.97	32.26	36.86	44.29	49.79	58.03
pc4h9	20.10[a]	78.46[b]	23.36[b]	29.12	34.13	38.46	45.45	50.65	58.64
hcchcch	119.30[c]	72.93[d]	20.83[d]	22.88	24.64	26.15	28.60	30.48	33.50
c-c6h7[e]	49.93	72.00	20.36	28.29	35.05	40.77	49.57	55.58	63.36
ch3cy24pd1[f]	54.11	76.68	23.40	31.10	37.40	42.51	50.03	55.06	62.36
ch3cy24pd[f]	25.08	70.96	21.93	30.19	37.10	42.85	51.59	57.61	66.26
ch3dcy24pd[f]	70.90	72.05	21.73	29.52	35.93	41.20	49.02	54.30	61.82
fulvene[g]	56.61	70.22	21.66	28.81	34.60	39.29	46.25	51.04	58.21
fulvenyl[f]	114.50	70.80	21.03	27.28	32.36	36.60	43.09	47.25	53.09

† pC_4H_9 (n-C_4H_9, 1-butyl, $CH_2CH_2CH_2CH_3$); sC_4H_9 (2-butyl, $CH_3CHCH_2CH_3$); c- (cyclic compound); c-C_6H_7 (1,3-cyclohexadienyl) fulvene ($CH_2C_5H_4$)

[a][26] [b][18] [c]See Text [d][17] [e][27] [f] Group Additivity [g]BAC-MP4

Table 2. Reaction Mechanism Rate Coefficients
($k_f = A\ T^b \exp(-E_a/RT)$, Units are moles, cm^3, seconds, K, and calories/mole)

REACTION	A	b	E_a	Reference
139.[α] c2h4(+m)=c2h2+h2(+m)[β]	1.80E+13	0.0	76000.0	[36]
Low pressure limit:	2.60E+17	0.0	79289.0	[37]
140. c2h4(+m)=c2h3+h(+m)	2.00E+16	0.0	110000.0	[38]
Low pressure limit:	3.80E+17	0.0	98168.0	[37]
143. c2h3+o2=ch2o+hco	1.70E+29	-5.312	6500.0	See Text
144. c2h3+o2=ch2hco+o	3.50E+14	-0.611	5260.0	See Text
145. c2h3+o2=c2h2+ho2	2.12E- 06	6.0	9484.0	[11]
165. c2h2+o2=hcco+oh	2.00E+07	1.5	30100.0	(a)
207. hcco+o2=co2+hco	2.40E+11	0.0	-854.0	[39] (b)
305. ac3h4+h=h2ccch+h2	2.00E+07	2.0	5000.0	[30] (c)
307. ac3h4+oh=h2ccch+h2o	1.00E+07	2.0	1000.0	[30] (c)
309. pc3h4+h=h2ccch+h2	2.00E+07	2.0	5000.0	[30] (c)
311. pc3h4+oh=h2ccch+h2o	1.00E+07	2.0	1000.0	[30] (c)
312. pc3h4+ch3=h2ccch+ch4	1.50E+00	3.5	5600.0	(c)
313. pc3h4+h=ch3+c2h2	5.12E+10	1.0	2060.0	(d)
329. h2ccch+h2ccch=c6h5+h	2.00E+12	0.0	0.0	(e)
332. chchcho+o2=c2h2+co+ho2	3.00E+12	0.0	0.0	(f)
342. c4h10=c2h5+c2h5	2.00E+16	0.0	81300.0	[41]
343. c4h10=nc3h7+ch3	1.74E+17	0.0	85700.0	[42] (g)
344. pc4h9[‡]+h=c4h10	5.00E+13	0.0	0.0	(h)
345. sc4h9[‡]+h=c4h10	5.00E+13	0.0	0.0	(h)
346. c4h10+o2=pc4h9+ho2	2.50E+13	0.0	49000.0	(h)
347. c4h10+o2=sc4h9+ho2	4.00E+13	0.0	47600.0	[43]
348. c4h10+ac3h5=pc4h9+c3h6	7.94E+11	0.0	20500.0	[42]
349. c4h10+ac3h5=sc4h9+c3h6	3.16E+11	0.0	16400.0	[42]
350. c4h10+ch3=pc4h9+ch4	5.00E+11	0.0	13600.0	[44]
351. c4h10+ch3=sc4h9+ch4	4.30E+11	0.0	10500.0	[44]
352. c4h10+h=pc4h9+h2	2.84E+05	2.54	6050.0	(i)
353. c4h10+h=sc4h9+h2	5.68E+05	2.40	3765.0	(i)
354. c4h10+oh=pc4h9+h2o	4.13E+07	1.73	753.0	[48]
355. c4h10+oh=sc4h9+h2o	7.23E+07	1.64	-247.0	[48]
356. c4h10+o=pc4h9+oh	1.13E+14	0.0	7850.0	[49] (j)
357. c4h10+o=sc4h9+oh	5.62E+13	0.0	5200.0	[49] (k)
358. c4h10+ho2=pc4h9+h2o2	1.70E+13	0.0	20460.0	[50]
359. c4h10+ho2=sc4h9+h2o2	1.12E+13	0.0	17700.0	[50]
360. sc4h9(+m)=c3h6+ch3(+m)	2.14E+12	0.65	30856.0	[26]
Low pressure limit:	6.32E+58	-12.85	35567.0	[26]
Enhanced Third Body Efficiencies:	h2o=5.0, h2=2.0, co2=3.0, co=2.0			
361. sc4h9=c4h8-1[‡]+h	2.00E+13	0.0	40400.0	[42]
362. sc4h9=c4h8-2[‡]+h	5.01E+12	0.0	37900.0	[42]
363. pc4h9(+m)=c2h5+c2h4(+m)	1.06E+13	0.0	27828.0	[26]
Low pressure limit:	1.897E+55	-11.91	32263.0	[26]
Enhanced Third Body Efficiencies:	h2o=5.0, h2=2.0, co2=3.0, co=2.0			
364. pc4h9=c4h8-1+h	1.26E+13	0.0	38600.0	[42]
365. c4h8-1=c2h3+c2h5	1.00E+19	-1.0	96770.0	(l)
366. c4h8-1=h+c4h7	4.11E+18	-1.0	97350.0	(m)
367. c4h8-1+ch3=c4h7+ch4	1.00E+11	0.0	7300.0	[42]
368. c4h8-1+h=c4h7+h2	5.00E+13	0.0	3900.0	[51]
369. c4h8-1+o=nc3h7+hco	1.80E+05	2.5	-1029.0	[52] (n)

REACTION	A	b	E_a	Reference
370. c4h8-1+o=ch2chcho+ch3+h	9.67E+04	2.5	-1029.0	[52] (n)
371. c4h8-1+oh=c4h7+h2o	2.25E+13	0.0	2217.0	[53]
372. c4h8-1+ac3h5=c4h7+c3h6	7.90E+10	0.0	12400.0	[42]
373. c4h8-1+o2=c4h7+ho2	4.00E+12	0.0	33200.0	[43] (o)
374. c4h8-2=h+c4h7	4.11E+18	-1.0	97350.0	(m)
375. c4h8-2+ch3=c4h7+ch4	1.00E+11	0.0	8200.0	[51]
376. c4h8-2+h=c4h7+h2	5.00E+13	0.0	3800.0	[51]
377. c4h8-2+o=ic3h7+hco	2.79E+06	2.12	-1775.0	[52] (p)
378. c4h8-2+oh=c4h7+h2o	3.90E+13	0.0	2217.0	(q)
381. c4h8-2+o2=c4h7+ho2	8.00E+13	0.0	37400.0	[43] (r)
384. c4h7+ch3=ch2chchch2+ch4	8.00E+12	0.0	0.0	[55]
385. c4h7+ac3h5=c3h6+ch2chchch2	6.31E+12	0.0	0.0	[55]
386. c4h7+o2=ch2chchch2+ho2	1.00E+09	0.0	0.0	[56] (s)
387. c4h7+h=ch2chchch2+h2	3.16E+13	0.0	0.0	[42]
391. ch2chchch2+o=ch2hco+c2h3	1.00E+12	0.0	0.0	(h)
434. hcchcch+c2h2=c6h5	9.60E+70	-17.77	31300.0	[35]
443. h2cccch(+m)=c4h2+h(+m)	1.00E+14	0.0	47000.0	(t)
Low pressure limit:	2.00E+15	0.0	40000.0	(t)
473. c-c5h5+c-c5h5=c10h8+h+h	2.00E+13	0.0	8000.0	(u)
572. indenyl+c-c5h5=phnthrn‡+h+h	1.00E+13	0.0	8000.0	1/2 k_{473}
582. ch3indenyl+c-c5h5=ch3phnthrn‡+h+h	1.00E+13	0.0	8000.0	1/2 k_{473}
631. benz(a)indene+c-c5h5=benz(a)phnthrn‡+h+h	1.00E+13	0.0	8000.0	1/2 k_{473}
662. hcco+o2=hco+co+o	2.50E+08	1.0	0.0	(v)
663. ac3h4+ch3=h2ccch+ch4	1.50E+00	3.5	5600.0	(d)
664. h2ccch+h2ccch=c6h6	5.56E+20	-2.535	1692.0	See k_{665}
665. h2ccch+ac3h5=fulvene+h+h	5.56E+20	-2.535	1692.0	(w)
666. c-c5h5+ch3=ch3cy24pd‡	1.76E+50	-11.0	18600.0	[62]
667. ch3cy24pd+h=c-c5h6+ch3	1.00E+13	0.0	1300.0	[62]
668. c6h6+h=ch3cy24pd1‡	2.39E+27	-3.92	29200.0	[62]
669. c-c6h7‡=ch3cy24pd1	5.00E+12	0.00	38100.0	[62]
670. ch3cy24pd1+h=ch3cy24pd	1.00E+14	0.00	0.0	[62]
671. ch3cy24pd1+h=c-c5h5+ch3	1.00E+14	0.00	0.0	[62]
672. c-c6h7=ch3dcy24pd‡	5.50E+10	0.00	28000.0	[62]
673. c6h6+h=c-c6h7	4.87E+56	-12.73	26800.0	[62]
674. ch3dcy24pd+h2=ch3cy24pd+h	4.00E+12	0.00	15000.0	[62]
675. fulvene=c6h6	9.84E+37	-7.40	76979.0	[63]
676. fulvene+h=c6h6+h	3.00E+12	0.50	2000.0	(x)
677. fulvene+h=fulvenyl+h2	3.03E+02	3.30	5690.0	(y)
678. fulvenyl+oh=fulvenyl+h2o	1.63E+08	1.42	1454.0	(y)
679. fulvenyl+h=benzene	1.00E+14	0.00	0.0	(z)
680. fulvenyl+o2=c-c5h4o+hco	1.00E+12	0.00	0.0	(aa)

$^{\alpha}$The reaction order is in accordance to Marinov [11].

$^{\beta}$ Fall - off reaction in the Lindemann - Hinshelwood form:

$$k = k_O[M]/(1+k_O[M]/k_\infty)$$

‡ phnthrn (phenanthrene); ch3phnthrn (methyl phenanthrene); benz(a)phnthrn (benz(a)phenanthrene); ch3cy24pd1 (methylcyclopentadienyl); ch3cy24pd (methyl cyclopentadiene); ch3dcy24pd (cyclopentadiene methyl radical); c-c6h7 (1,3-cyclohexadienyl) ; fulvene (ch2c5h4)

(a) Reduced A-factor by a factor of 10.

(b) Rate expression was adjusted downward to within the prescribed uncertainty factor of ten as cited in [39]. Products assigned as suggested in [30].

(c) Rate expression adjusted in accordance to H-atom abstraction reactions for Propene + X, where X = {OH,H,CH_3}.

(d) Transition state theory fit to Whytock data [40].

(e) Rate constant adjusted downward from 3.0E+12 cm^3/mol/sec so as to include a second aromatic producing channel from propargyl recombination.

(f) Perferred products than those listed in [11].

(g) A-factor adjusted downward a factor of 1.8.

(h) Estimate.

(i) Rate expressions for c4h10+h=sc4h9+h2 and c4h10+h=pc4h9+h2 were obtained by fitting data from [45-47] and using the relation of $k_{primary}/k_{secondary} = 0.509T^{0.14}exp(-1150K/T)$ as obtained from [31] for abstraction reactions by H-atoms involving primary and secondary hydrogens of propane with corrections made for reaction path degeneracies.

(j) Analogy with Ethane + O.

(k) Subtracted the Ethane + O rate constant from the Propane + O to obtain a rate constant for abstraction of secondary H-atoms.

(l) Forward rate calculated from a reverse rate constant of 9.0E+12 and microscopic reversibility.

(m) Forward rate calculated from a reverse rate constant of 5.0E+13 and microscopic reversibility.

(n) Estimated from rate constant of 1-Butene + O. Products assumed.

(o) Assumed activation energy is equal to enthalpy of reaction at 298K. A-factor reduced from 4.0E+13 [43] because of loss of rotor in transistion state for the case of allyl C-H.

(p) Estimated from rate constant of cis-2-butene + O = products and trans-2-butene + O = products. Products assumed.

(q) The activation energy is assumed to be the same as c4h8-1+oh=c4h7+h2o. The A-factor was obtained from [54] with rate constant evaluated at 1200K.

(r) A-factor twice c3h6+o2=ac3h5+ho2 because 2-c4h8 has twice as many allylic C-H bonds as propene. Activation energy is equal to enthalpy of reaction at 298K.

(s) Analogy with c5h9+o2 = penta-1,3-diene+ho2. Rate constant adjusted downward a factor of 3. Activation energy assumed to be zero.

(t) Activation energy for the high and low pressure limits were adjusted downward by 8.0kcal/mol to reflect the change in the heat of formation value assigned to h2cccch.

(u) The activation energy was adjusted in accordance to [57]. We have assumed the rate limiting step to naphthalene production is the 8.0kcal/mol intrinsic activation energy barrier associated with the scissioning of the first H-atom. See Text.

(v) Rate expression is based on [30] with assigned products of choco (glyoxal radical)+o. We have assumed choco automatically decomposes to hco and co, hence the products found in reaction 662.

(w) This rate expression was obtained from allyl recombination data of [58-60]. This rate expression is assumed to represent the lower limit kinetic rate for the allyl+propargyl reaction to products at one atmosphere. We have also assumed the rate controlling step for this reaction occurs at the entrance channel with 100% conversion to cyclic products based on the experimental findings of Huntsman [61]. This rate expression was also extended to reaction 664.

(x) Assumed rate expression based on findings of [57].

(y) Rate expression based on analogous reactions of Benzene+X, where X = {OH,H}.

(z) Rate constant assignment was estimated.

(aa) Vinylic compounds react with O_2 at a rate constant of ca. 1.0E+12 to 1.0E+13 cm^3/mol/sec. Products assumed.

Figure Captions

Figure 1. Comparison of model predictions with experimental concentration profiles in the n-butane flame. Symbols represent the experimental measurements and the lines represent the model predictions. (a) Comparison to C_4H_{10}, O_2, H_2O and the radiation corrected temperature profile used. (b) Comparison to CO, CO_2, and H_2.

Figure 2. Comparison of model predictions with experimental concentration profiles in the n-butane flame. Symbols represent the experimental measurements and the lines represent the model predictions. (a) Comparison to CH_4, C_2H_2, C_2H_4, and C_2H_6. (b) Comparison to C_3H_4, C_4H_2, and C_4H_4. Numerical computations shown for C_3H_6.

Figure 3. Reaction flux/pathway diagram for the two important reaction sequences leading to reaction intermediates and combustion byproducts that occur in the n-butane-oxygen-argon flame. Species shown in shadowed italics are resonantly stabilized free radicals.

Figure 4. Reaction flux/pathway diagram for the important pathways leading to aromatic and polycyclic aromatic hydrocarbon formation in the n-butane-oxygen-argon flame. Species shown in shadowed italics are resonantly stabilized free radicals.

Figure 5. Reaction flux/pathway diagram for the important pathways leading to aromatic, branched aromatic, and polycyclic aromatic hydrocarbon formation in the n-butane-oxygen-argon flame. Species shown in shadowed italics are resonantly stabilized free radicals.

Figure 6. Comparison of model predictions with experimental concentration profiles in the n-butane flame. Symbols represent the experimental measurements and the lines represent the model predictions. (a) Comparison to benzene (C_6H_6), naphthalene ($C_{10}H_8$), and cyclopentadiene (c-C_5H_6). (b) Comparison to toluene ($C_6H_5CH_3$), ethylbenzene ($C_6H_5C_2H_5$), styrene ($C_6H_5C_2H_3$), and phenyl acetylene ($C_6H_5C_2H$).

Figure 7. (a) Normalized sensitivity coefficients computed for propargyl (H_2CCCH) and (b) Normalized sensitivity coefficients computed for benzene (C_6H_6) across the n-butane flame.

Figure 8. (a) Normalized sensitivity coefficients computed for cyclopentadienyl (c-C_5H_5) and (b) Normalized sensitivity coefficients computed for naphthalene ($C_{10}H_8$) across the n-butane flame.

Figure 9. Comparison of model predictions with experimental concentration profiles in the n-butane flame. Symbols represent the experimental measurements and the lines represent the model predictions. (a) Comparison to phenanthrene, anthracene, acenaphthalene, and pyrene. (b) Comparison to o-xylene, indene, biphenyl, and fluoranthene. Note: Logarithmic scale used in figures 9(a) and 9(b).

Figure 10. Comparison of model predictions with experimental concentration profiles in the n-butane flame. Symbols represent the experimental measurements and the lines represent the model predictions. (a) Comparison to 9H-fluorene, 4H-cyclopent(def)phenanthrene, and benzo(ghi)fluoranthrene. No comparison is shown for cyclo(cd)pyrene (experimental data only). (b) Experimental concentration profiles (symbols) of Azulene, Biphenylene, 1-HPhenalene, and Benzo(a)pyrene in the n-butane flame. Note: Logarithmic scale used in figures 10(a) and 10(b).

Figure 11. (a) Model prediction of the H, CH_3, C_2H_3, aC_3H_5 and H_2CCCH concentrations in the n-butane flame. (b) Model prediction of the H_2CCCCH, CH_3CCCH_2,CH_2CHCCH_2, and C_4H_7 concentrations in the n-butane flame. Note: Logarithmic scale used in figures 11(a) and 11(b).

Figure 12. Model prediction of the cyclopentadienyl (c-C_5H_5), phenyl (C_6H_5), phenoxy (C_6H_5O), benzyl ($C_6H_5CH_2$), Indenyl (C_9H_7) concentrations in the n-butane flame. Note: Logarithmic scale used in the figure.

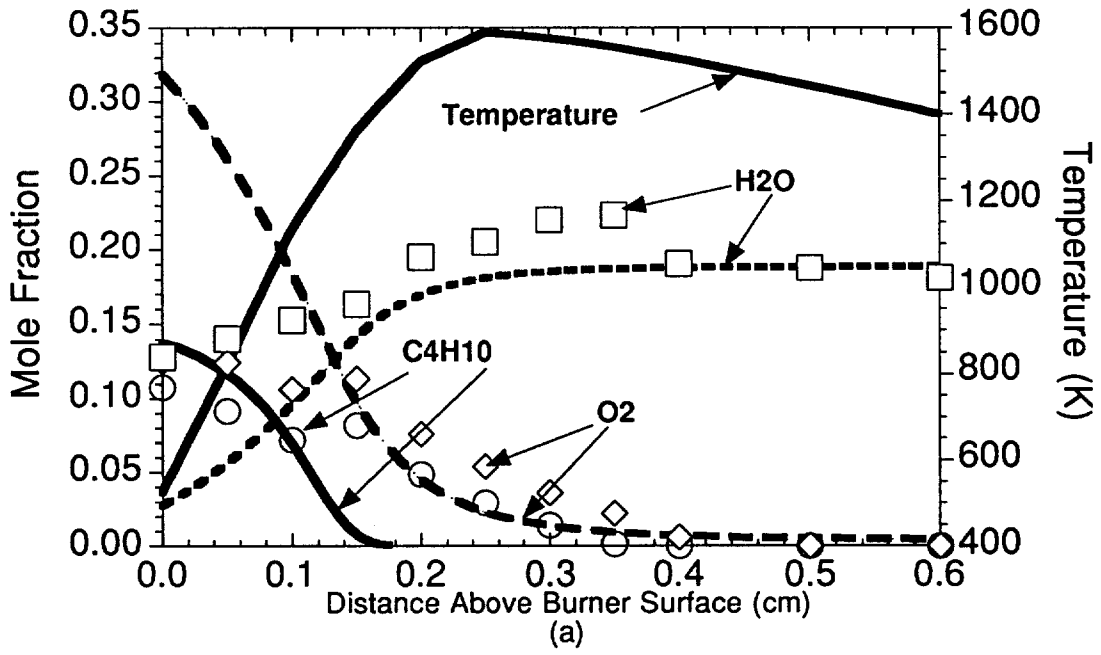
Mole Fraction
Temperature (K)
Temperature
H2O
C4H10
O2
Distance Above Burner Surface (cm)
(a)

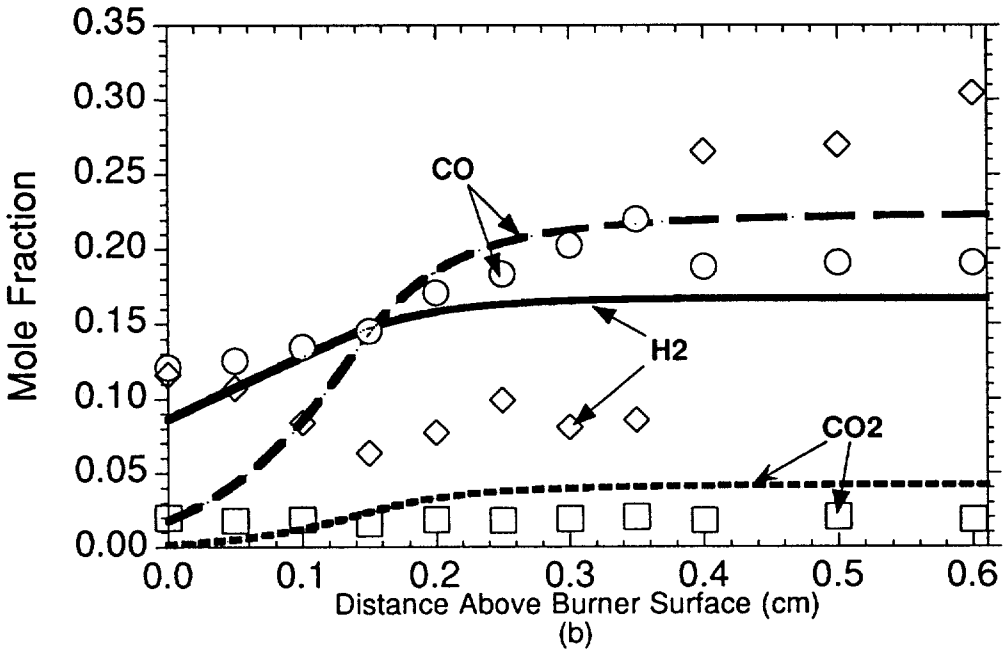
Mole Fraction
CO
H2
CO2
Distance Above Burner Surface (cm)
(b)

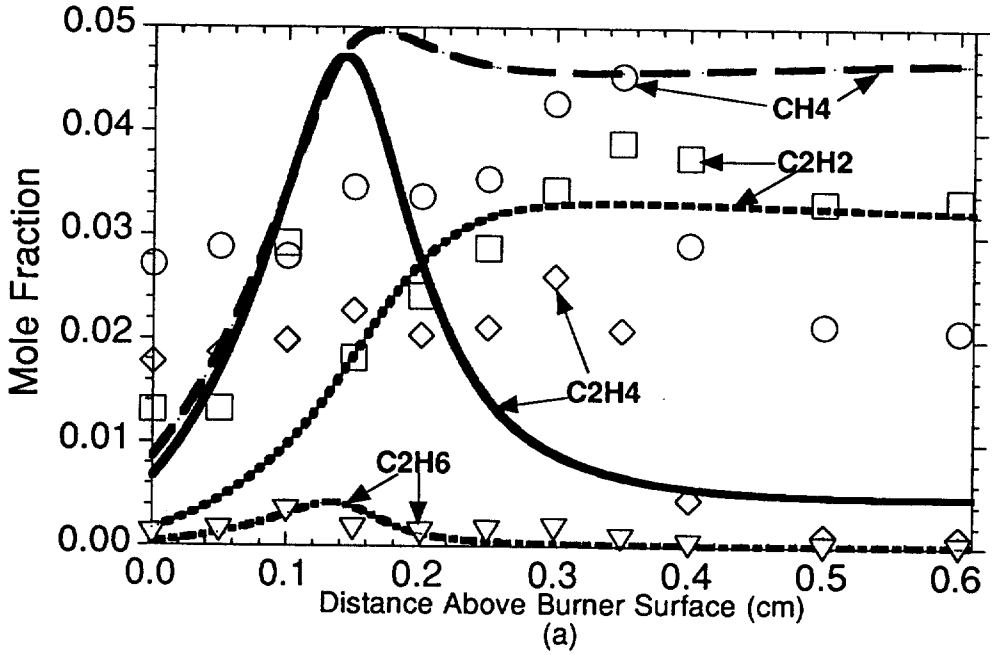
0.05
0.04
0.03
0.02
0.01
0.00
Mole Fraction
CH4
C2H2
C2H4
C2H6
0.0
0.1
0.2
0.3
0.4
0.5
0.6
Distance Above Burner Surface (cm)
(a)

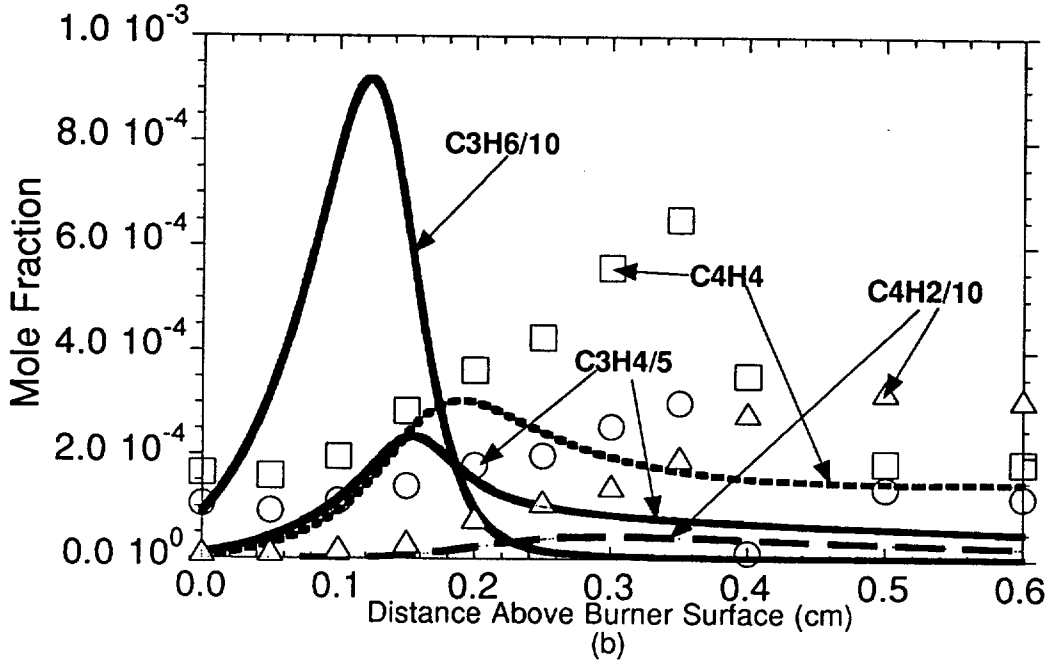
1.0 10-3
8.0 10-4
6.0 10-4
4.0 10-4
2.0 10-4
0.0 100
Mole Fraction
C3H6/10
C4H4
C4H2/10
C3H4/5
0.0
0.1
0.2
0.3
0.4
0.5
0.6
Distance Above Burner Surface (cm)
(b)

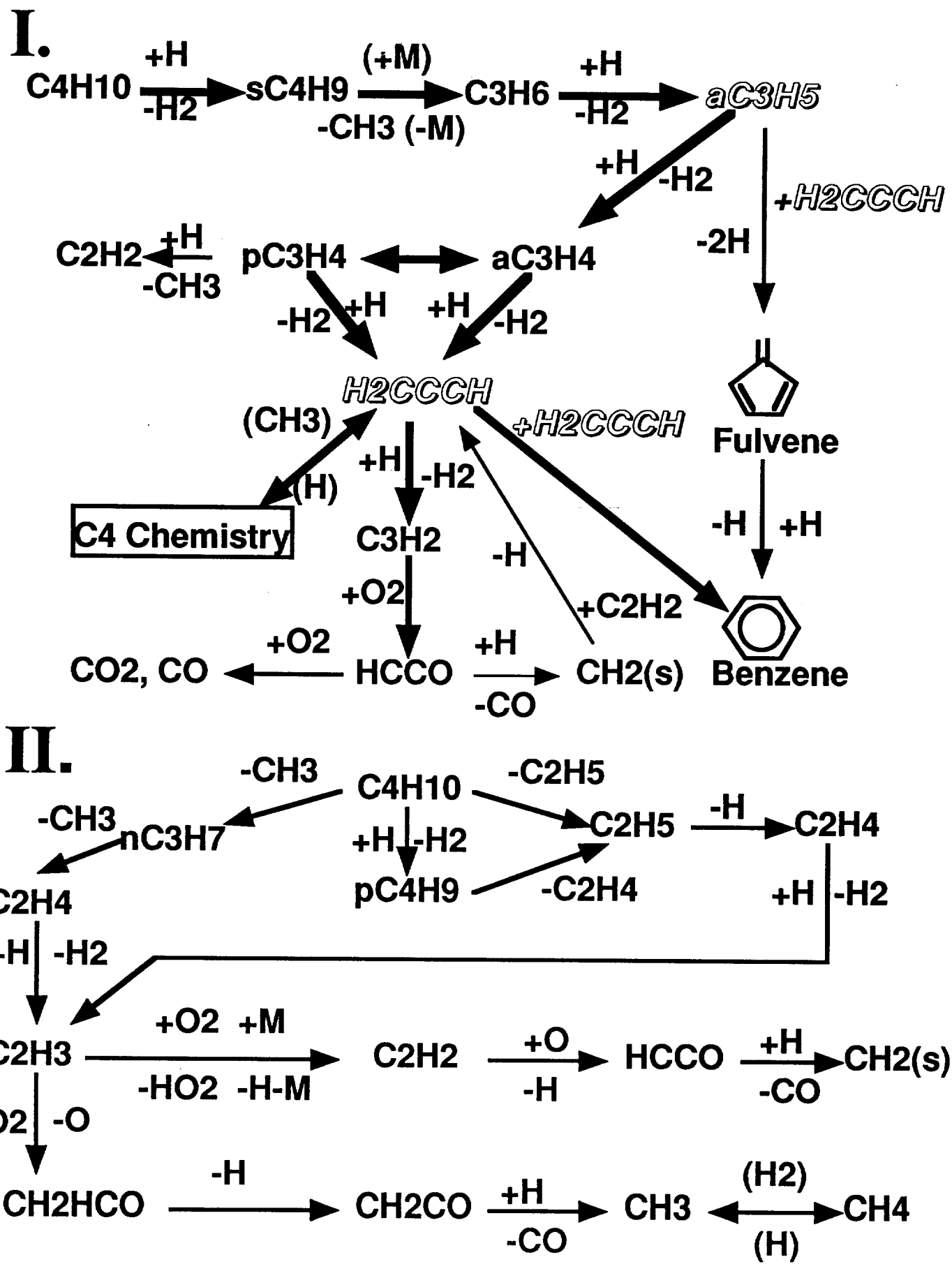
I.
C4H10
+H
-H2
sC4H9
(+M)
-CH3 (-M)
C3H6
+H
-H2
aC3H5
+H
-H2
+H2CCCH
-2H
C2H2
+H
-CH3
pC3H4
aC3H4
-H2
+H
+H
-H2
H2CCCH
(CH3)
(H)
+H2CCCH
Fulvene
+H
-H2
C4 Chemistry
C3H2
-H
+O2
+C2H2
-H
+H
+O2
CO2, CO
HCCO
CH2(s)
-CO
Benzene
II.
-CH3
C4H10
-C2H5
-CH3
nC3H7
+H
-H2
C2H5
-H
C2H4
C2H4
pC4H9
-C2H4
+H
-H2
+H
-H2
C2H3
+O2
+M
-HO2
-H-M
C2H2
+O
-H
HCCO
+H
-CO
CH2(s)
+O2
-O
CH2HCO
-H
CH2CO
+H
-CO
CH3
(H2)
(H)
CH4

Fig. 3

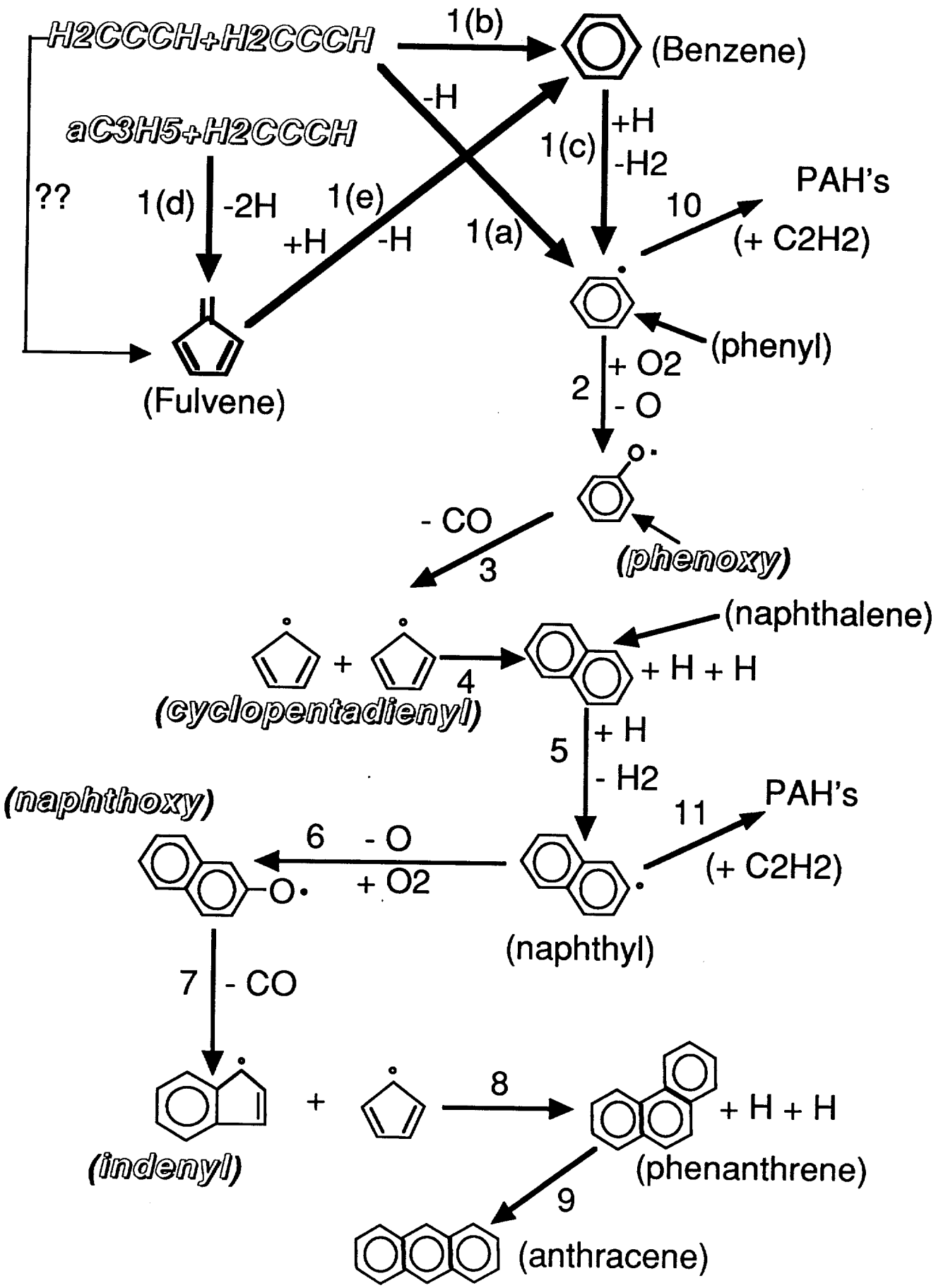
H2CCCH+H2CCCH
1(b)
(Benzene)
-H
aC3H5+H2CCCH
1(c)
+H
-H2
??
1(d)
-2H
1(e)
+H
-H
1(a)
10
PAH's
(+ C2H2)
(phenyl)
(Fulvene)
+ O2
2
- O
- CO
3
(phenoxy)
(naphthalene)
+
4
+ H + H
(cyclopentadienyl)
5
+ H
- H2
(naphthoxy)
11
PAH's
6
- O
+ O2
(+ C2H2)
(naphthyl)
7
- CO
8
+
+ H + H
(indenyl)
(phenanthrene)
9
(anthracene)

Fig. 4

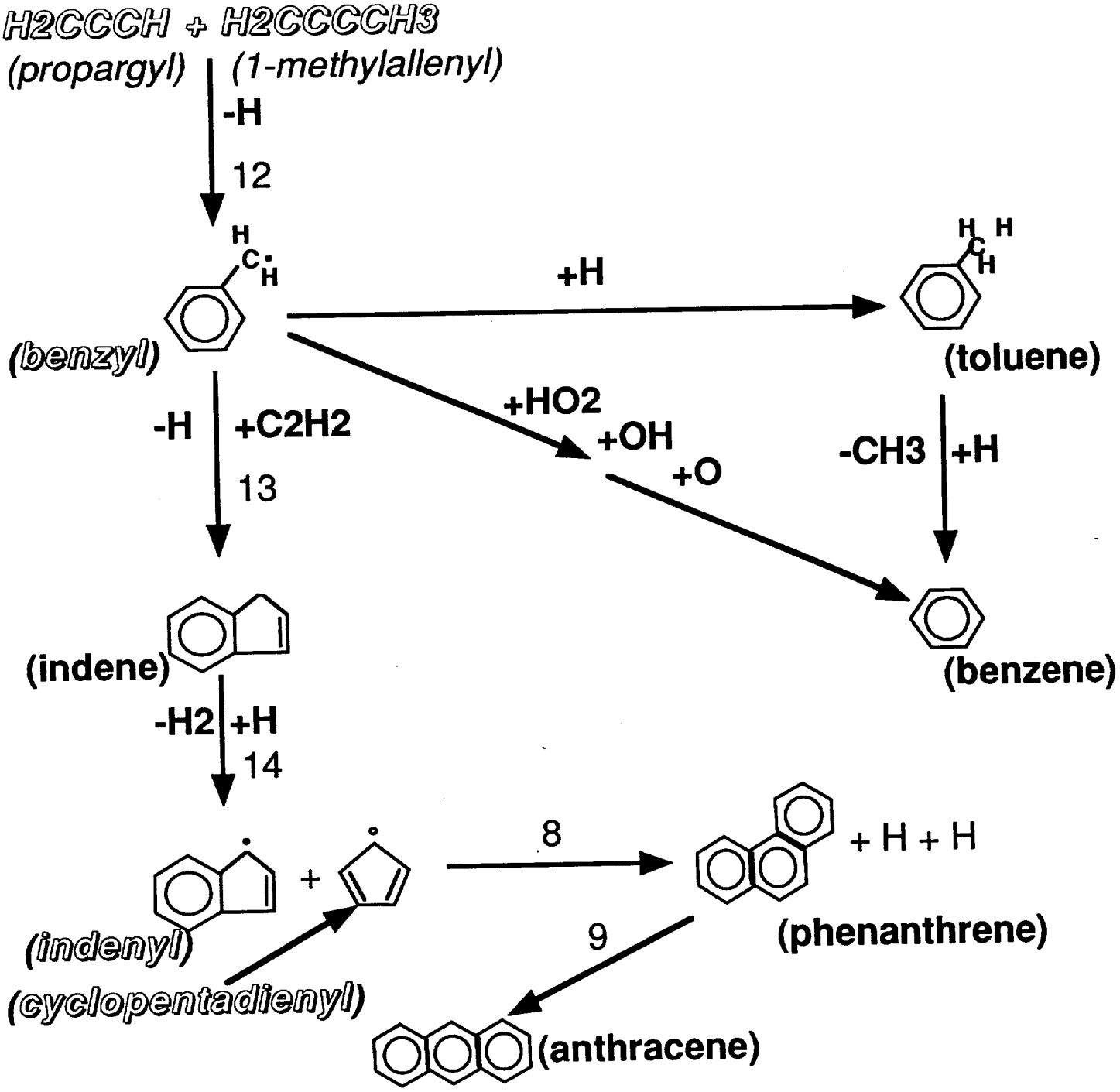
H2CCCH + H2CCCCH3
(propargyl)
(1-methylallenyl)
-H
12
(benzyl)
+H
(toluene)
-H
+C2H2
13
+HO2
+OH
+O
-CH3
+H
(indene)
(benzene)
-H2
+H
14
8
+ H + H
(indenyl)
(cyclopentadienyl)
(phenanthrene)
9
(anthracene)

Fig. 5

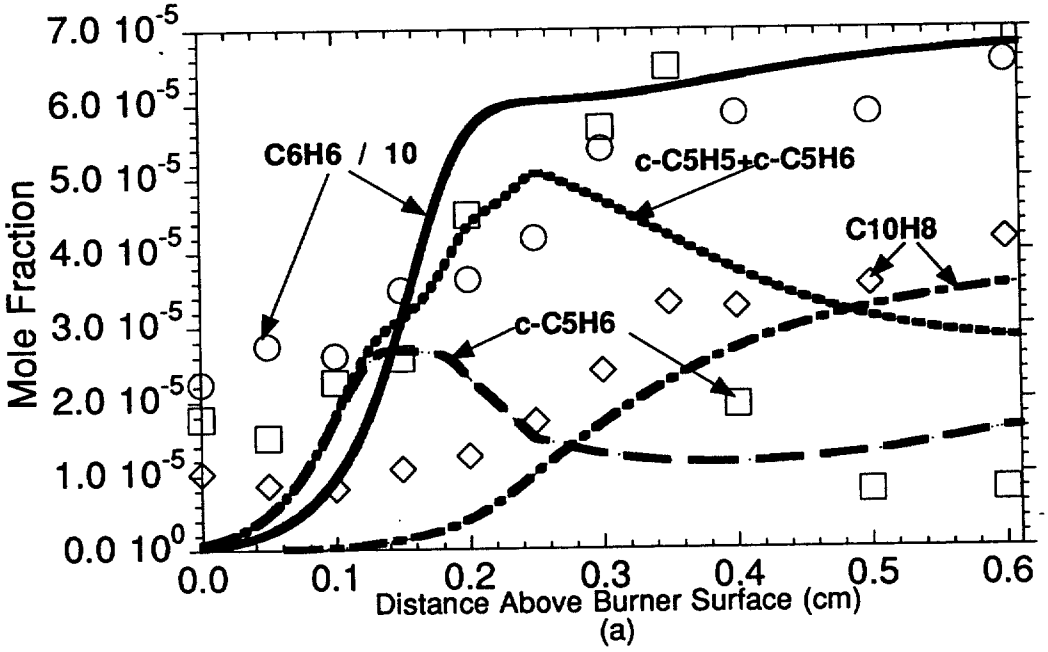
7.0 10-5
6.0 10-5
5.0 10-5
4.0 10-5
3.0 10-5
2.0 10-5
1.0 10-5
0.0 100
Mole Fraction
C6H6 / 10
c-C5H5+c-C5H6
C10H8
c-C5H6
0.0
0.1
0.2
0.3
0.4
0.5
0.6
Distance Above Burner Surface (cm)
(a)

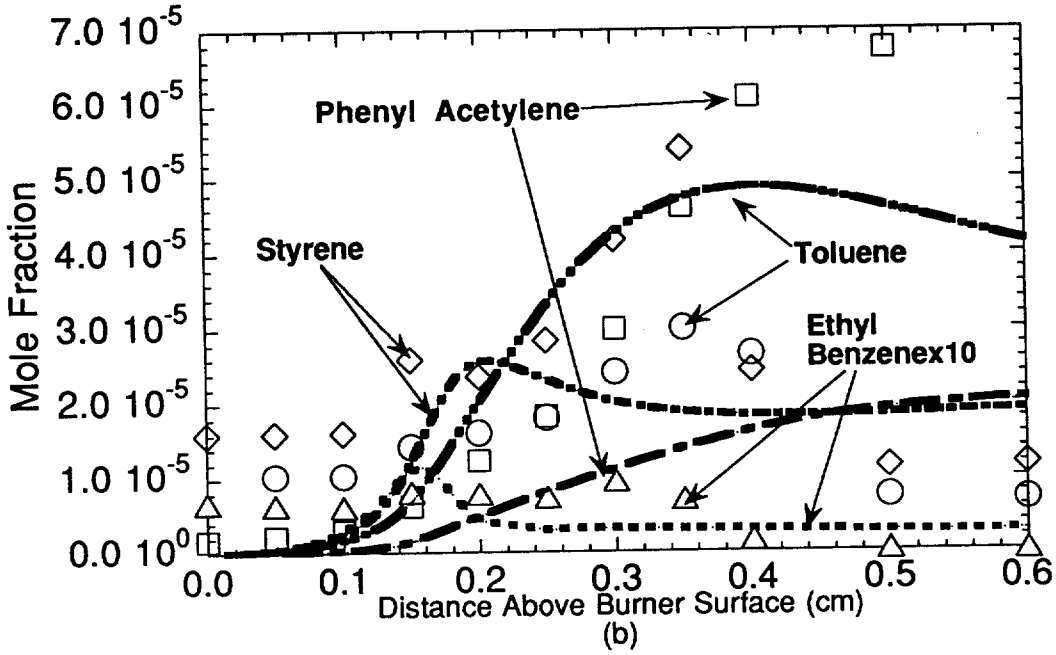
7.0 10-5
6.0 10-5
5.0 10-5
4.0 10-5
3.0 10-5
2.0 10-5
1.0 10-5
0.0 100
Mole Fraction
Phenyl Acetylene
Styrene
Toluene
Ethyl Benzenex10
0.0
0.1
0.2
0.3
0.4
0.5
0.6
Distance Above Burner Surface (cm)
(b)

Fig 6

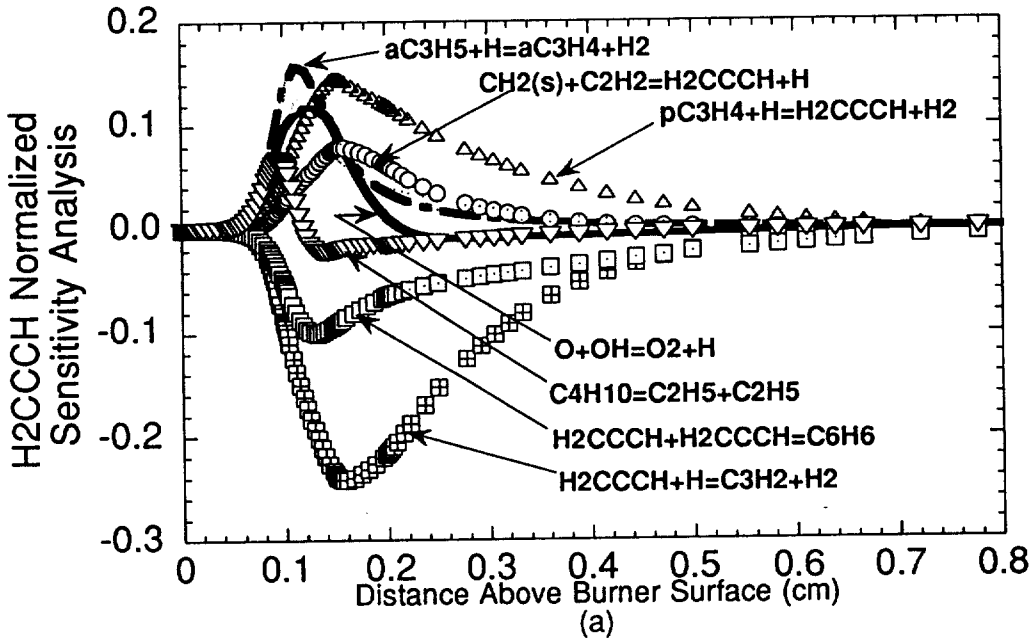
H2CCCH Normalized Sensitivity Analysis
0.2
0.1
0.0
-0.1
-0.2
-0.3
aC3H5+H=aC3H4+H2
CH2(s)+C2H2=H2CCCH+H
pC3H4+H=H2CCCH+H2
O+OH=O2+H
C4H10=C2H5+C2H5
H2CCCH+H2CCCH=C6H6
H2CCCH+H=C3H2+H2
0
0.1
0.2
0.3
0.4
0.5
0.6
0.7
0.8
Distance Above Burner Surface (cm)
(a)

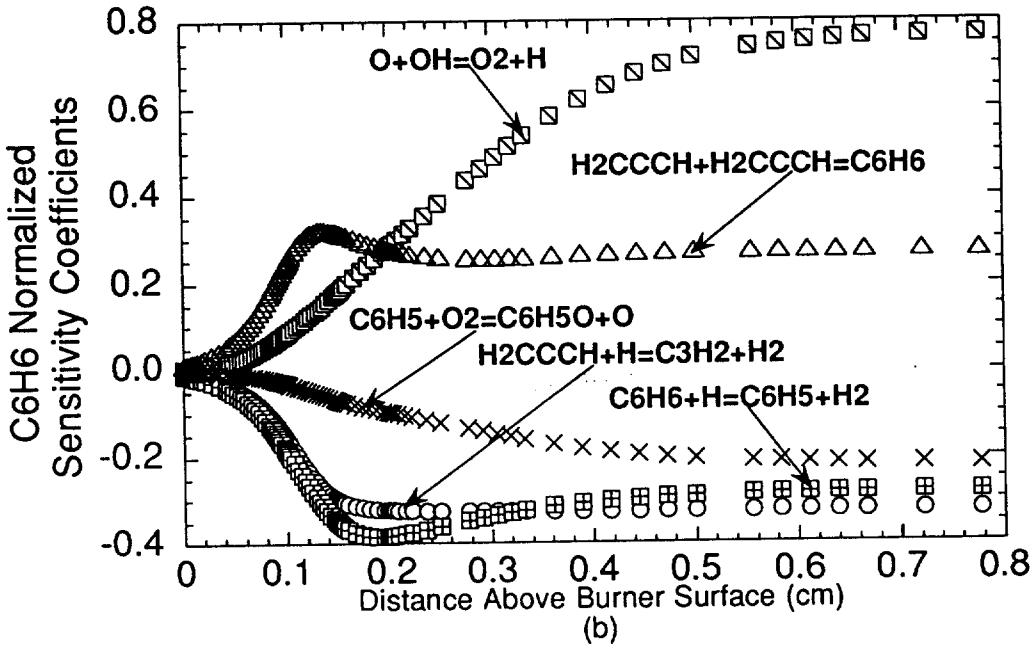
C6H6 Normalized Sensitivity Coefficients
0.8
0.6
0.4
0.2
0.0
-0.2
-0.4
O+OH=O2+H
H2CCCH+H2CCCH=C6H6
C6H5+O2=C6H5O+O
H2CCCH+H=C3H2+H2
C6H6+H=C6H5+H2
0
0.1
0.2
0.3
0.4
0.5
0.6
0.7
0.8
Distance Above Burner Surface (cm)
(b)

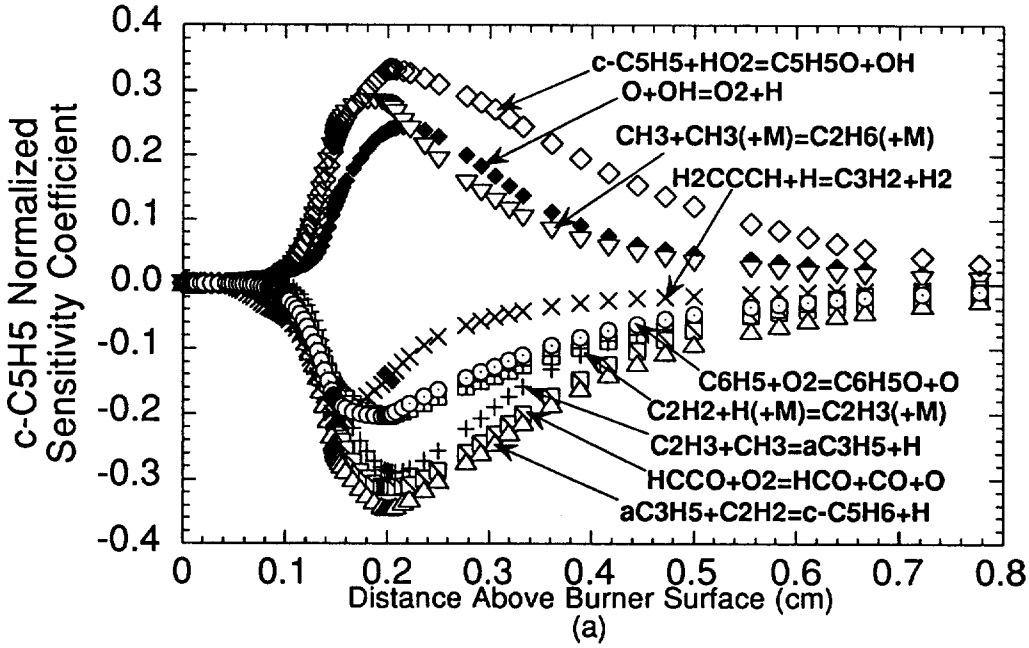
c-C5H5 Normalized Sensitivity Coefficient
Distance Above Burner Surface (cm)
c-C5H5+HO2=C5H5O+OH
O+OH=O2+H
CH3+CH3(+M)=C2H6(+M)
H2CCCH+H=C3H2+H2
C6H5+O2=C6H5O+O
C2H2+H(+M)=C2H3(+M)
C2H3+CH3=aC3H5+H
HCCO+O2=HCO+CO+O
aC3H5+C2H2=c-C5H6+H
(a)

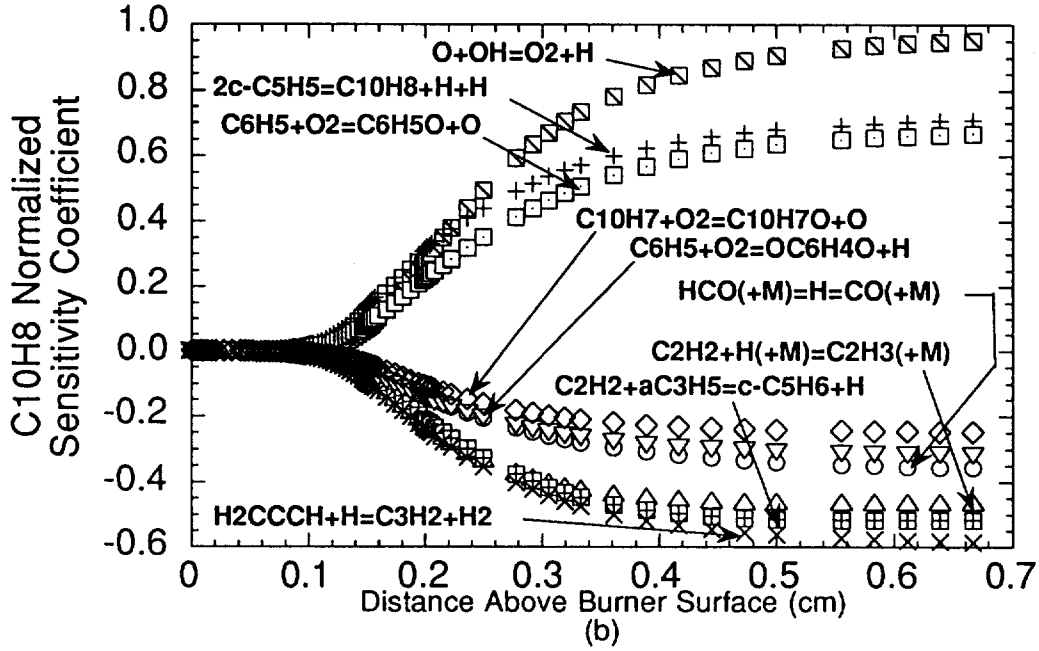
C10H8 Normalized Sensitivity Coefficient
Distance Above Burner Surface (cm)
O+OH=O2+H
2c-C5H5=C10H8+H+H
C6H5+O2=C6H5O+O
C10H7+O2=C10H7O+O
C6H5+O2=OC6H4O+H
HCO(+M)=H=CO(+M)
C2H2+H(+M)=C2H3(+M)
C2H2+aC3H5=c-C5H6+H
H2CCCH+H=C3H2+H2
(b)

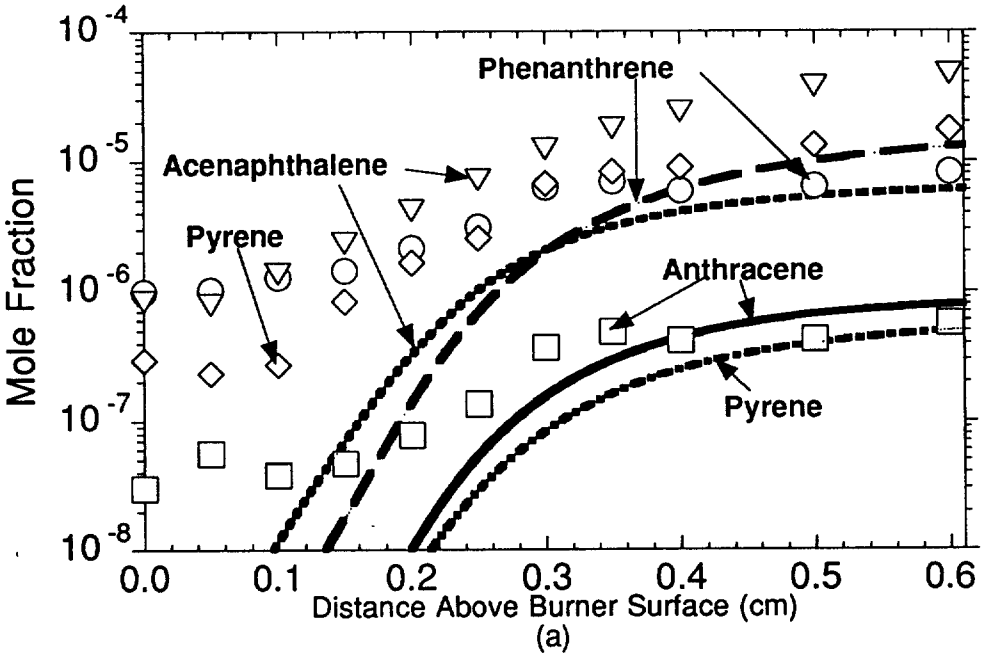
Phenanthrene
Acenaphthalene
Pyrene
Anthracene
Pyrene
Mole Fraction
Distance Above Burner Surface (cm)

(a)

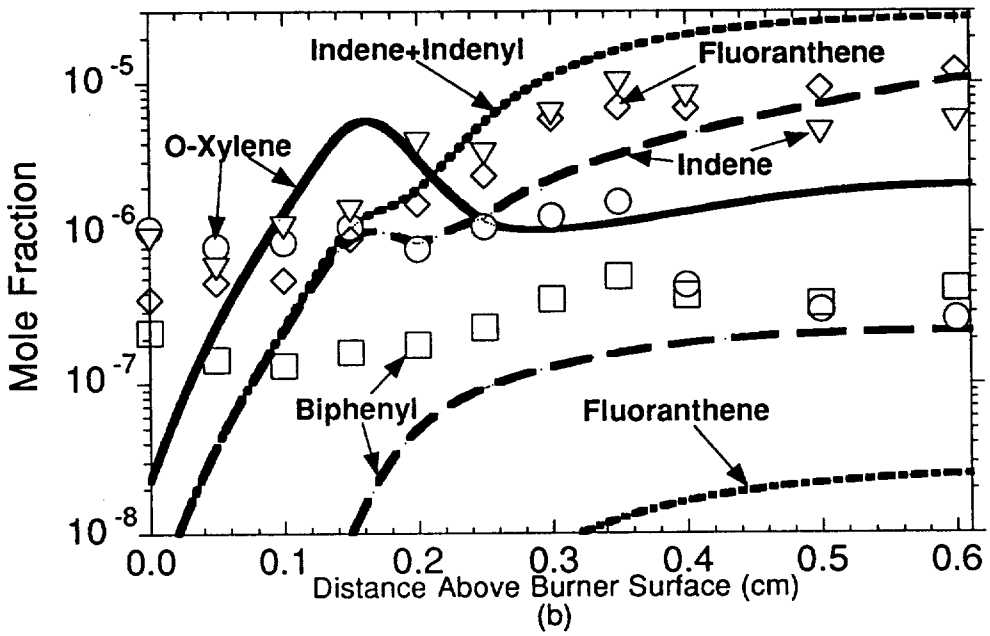
Indene+Indenyl
Fluoranthene
O-Xylene
Indene
Biphenyl
Fluoranthene
Mole Fraction
Distance Above Burner Surface (cm)

(b)

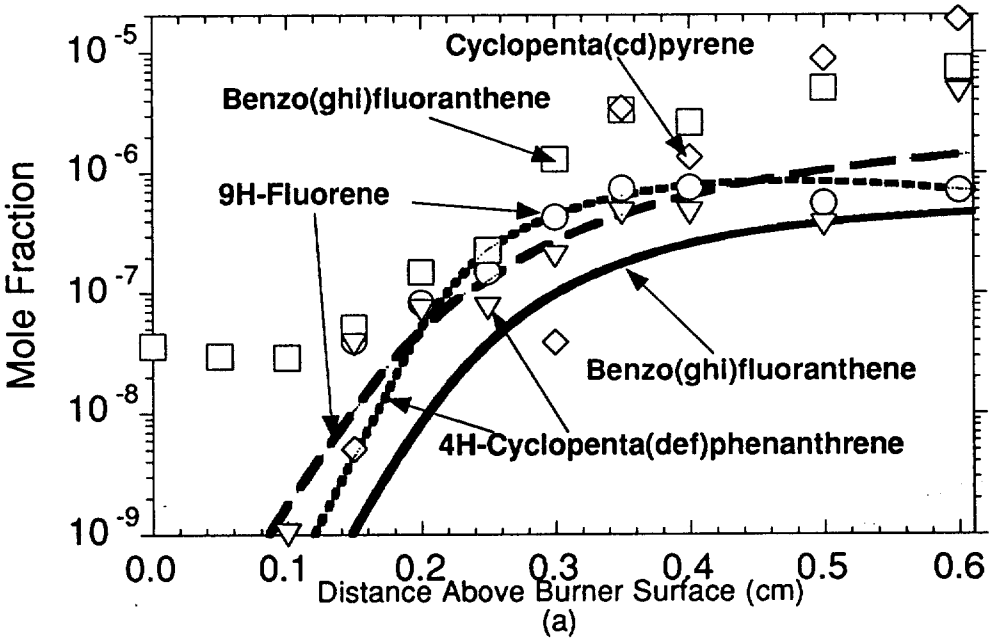
Cyclopenta(cd)pyrene
Benzo(ghi)fluoranthene
9H-Fluorene
Benzo(ghi)fluoranthene
4H-Cyclopenta(def)phenanthrene
Mole Fraction
Distance Above Burner Surface (cm)
(a)

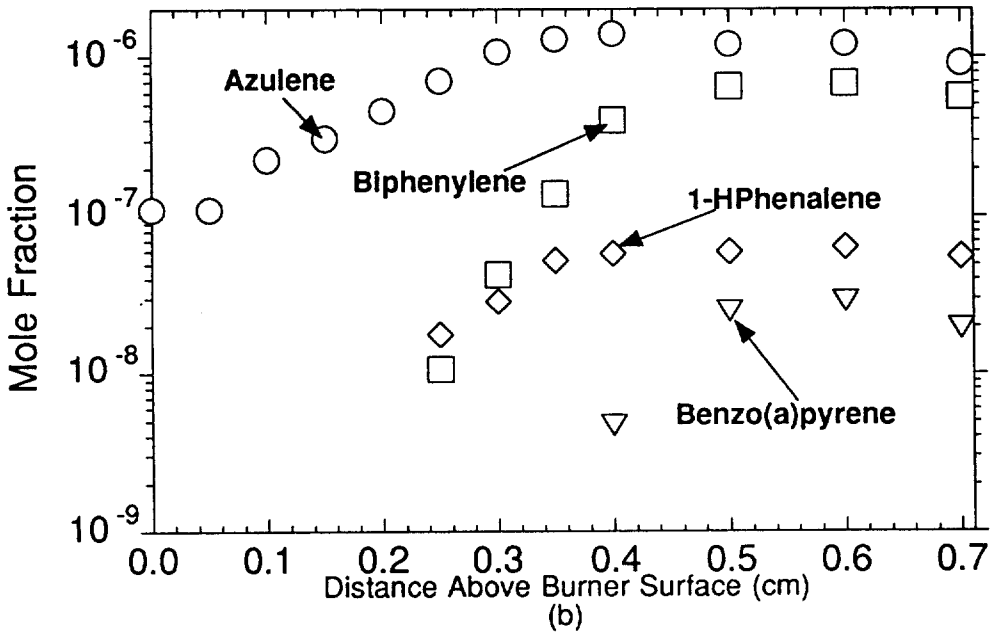
Azulene
Biphenylene
1-HPhenalene
Benzo(a)pyrene
Mole Fraction
Distance Above Burner Surface (cm)
(b)

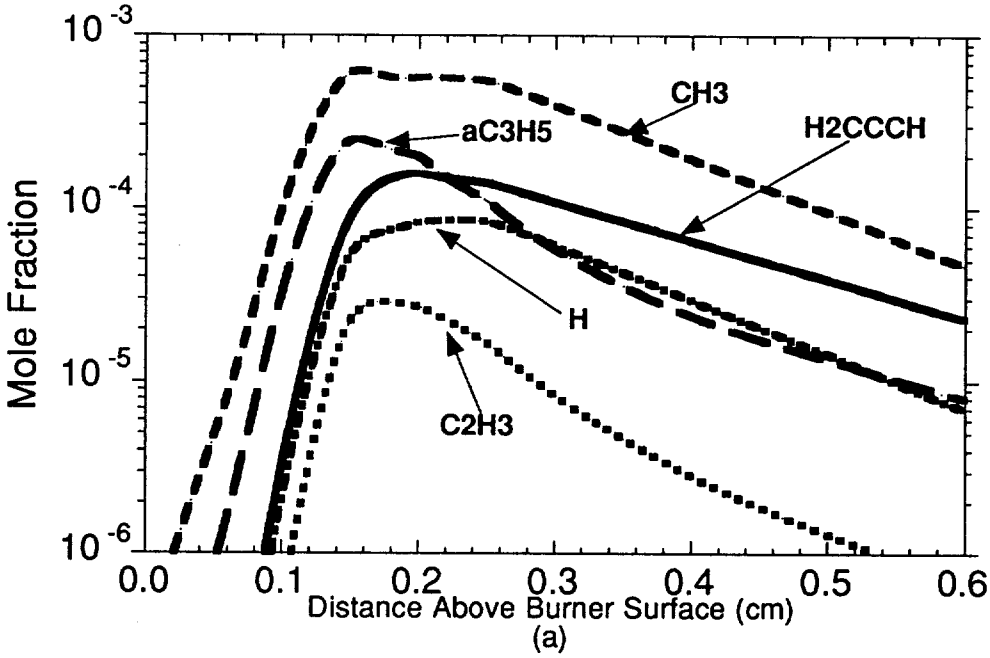
10 -3
10 -4
10 -5
10 -6
Mole Fraction
CH3
aC3H5
H2CCCH
H
C2H3
0.0
0.1
0.2
0.3
0.4
0.5
0.6
Distance Above Burner Surface (cm)
(a)

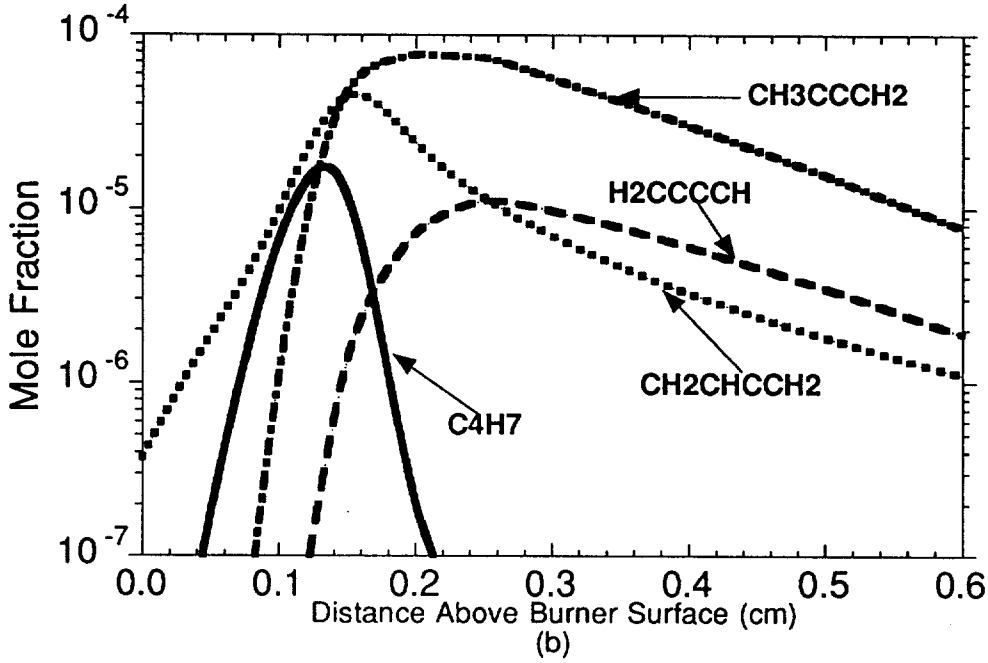
10 -4
10 -5
10 -6
10 -7
Mole Fraction
CH3CCCH2
H2CCCCH
CH2CHCCH2
C4H7
0.0
0.1
0.2
0.3
0.4
0.5
0.6
Distance Above Burner Surface (cm)
(b)

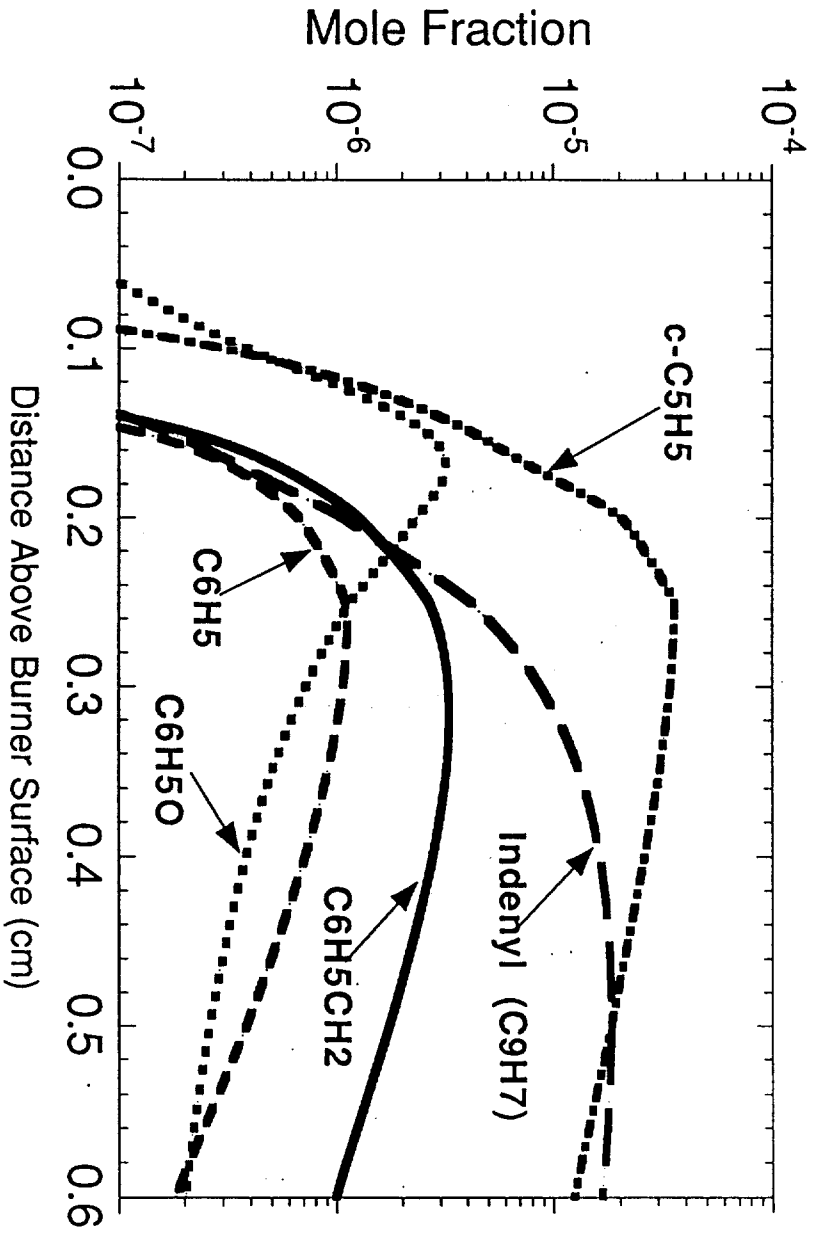
Mole Fraction
10-4
10-5
10-6
10-7
0.0
0.1
0.2
0.3
0.4
0.5
0.6
Distance Above Burner Surface (cm)
c-C5H5
C6H5
C6H5O
C6H5CH2
Indenyl (C9H7)

Fig 12